Title
Measurement of the effect of force on the helix-coil transition using hybrid smFRET-magnetic tweezers

Author
Leachman, Samuel Matthias

Publication Date
2015

Measurement of the effect of force on the helix-coil transition using hybrid smFRET-magnetic tweezers

By

Samuel Matthias Leachman

A dissertation submitted in partial satisfaction of the

requirements for the degree of

Doctor of Philosophy

in

Chemistry

in the

Graduate Division

of the

University of California, Berkeley

Committee in charge:

Professor Susan Marqusee, Co-Chair
Professor Carlos J. Bustamante, Co-Chair
Professor Judith P. Klinman
Professor Daniel Alden Fletcher

Fall 2015

Abstract

Measurement of the effect of force on the helix-coil transition using hybrid smFRET-magnetic tweezers

By

Samuel Matthias Leachman

Doctor of Philosophy in Chemistry

University of California, Berkeley

Professor Susan Marqusee and Professor Carlos Bustamante, Co-Chairs

The alpha helix is the predominant element of secondary structure in proteins and is involved in a number of force-dependent biological processes. Despite its importance, direct measurements of its response to force have not been made. Investigations of the mechanical properties of biomolecules usually rely on force spectroscopic techniques such as optical tweezers or atomic force spectroscopy, but these techniques have failed to detect the unfolding/folding signature of the alpha helix, presumably because the cooperativity of the helix-coil transition is broad and the expected extension change is small.

This research describes the development of an instrument combining magnetic tweezers and total internal reflection fluorescence microscopy (TIRF) with the goal of capturing the effect of force on an isolated alpha helix. Changes in extension are reported by single-molecule Förster resonance energy transfer (smFRET) between small-molecule fluorophores conjugated near the middle of such a helix. This technique provides an extremely sensitive probe of conformation that is unaffected by the DNA handles typically used in optical tweezers experiments and is amenable to both nucleic acid and protein constructs. Calibration is performed and verified using the known worm-like chain (WLC) force-extension behavior of DNA, its overstretching transition, and the opening and closing of a previously characterized DNA hairpin.

Using this instrument, the alpha helix is observed to unfold cooperatively and reversibly from 11 pN to 17 pN, indicating rapid equilibrium between the helix and coil states. This contrasts with the behavior of an unstructured polypeptide that exhibits a steady, non-cooperative FRET decrease across the 1-30 pN range of applied force. The behavior of the unstructured polypeptide is well described by a WLC model, reformulated here in terms of root-mean square displacement. The helix-prediction algorithm AGADIR, when modified to incorporate the effect of force and a WLC model of the unfolded state, successfully explains the observed folding signature of the alpha helix.

Acknowledgements

First and foremost, I would like to thank my advisors, Susan and Carlos, for their mentorship and financial support over the last six and a half years. They are experts in scientific reasoning and communication, and the tremendous positive impact they had on me is evident from what I've been able to accomplish here. I am indebted to them for teaming me up with Yito Wilson, who stands out as the most dedicated, careful, and courteous researcher I've ever met. Over the many hours we spent together in Stanley Hall B308A, he taught me some important truths: Hard work and sacrifice produce more breakthroughs than luck. Celebrate and remember the days when things work. Strive for N=3, because once is an anomaly and twice is a coincidence. Yito single-handedly developed the labeling strategy that allowed us to make the first single-molecule force-FRET measurement on a protein. Getting to that point required such considerable persistence, optimism, and technical skill that I can comfortably say that this dissertation would not have been possible without him.

Every argument presented here has been honed through impassioned lab meeting discussion, and I'm grateful to all my colleagues in both labs for engaging in this over the years. A few deserve special mention: Jesse Dill, my first mentor, who vouched for me early on; the exceedingly knowledgeable Avi Samelson, whom I bounced many ideas off; Bernie Cervantes, the best undergraduate research assistant we could've asked for; Troy Lionberger, who brought a renewed sense of community to the lab; and Heekyung Kim, who built the TIRF microscope and trained Yito and me in its use. I credit her specifically for the excitation and emission diagrams in this dissertation. Similarly, I credit Yito for the diagram of his hairpin functionalization scheme. I'm grateful to all the members of the Marqusee Lab I've worked with over the years: Phillip, Diane, Kambiz, Bharat, Emily, Eric, Sabriya, Laura, Diana, Brendan, Emma, Helen, Madeleine, Shion, Charlotte, Mia, Rachel, Greg, Katelyn, Katie Hart, Geoff, Santosh, Katherine, and Katie Tripp. Numerous former and current members of the Bustamante Lab deserve thanks as well: Steve Smith, Charlie, Craig, Gheorghe, Pim, Dan, Maya, Varsha, Lisa, Antony, Cristhian, César, Mau, Shannon, Clement, Filipp, Ronen, Mina, Wee, Bibiana, Christian Kaiser, Ninning, Shixin, Tingting, Ariel, Aathi, Toyotaka, Hendrik, Yumeng, and others.

Numerous people outside lab gave me the encouragement I needed to see this through, including my parents Ron and Trudy, my brothers Ben, Nate, and Jed, my partner Kim, and many reliable friends. Alex and Nick, hang in there. The UC Berkeley Symphony Orchestra was very important to me during my time here, and I want to thank every member, especially director David Milnes, for giving me a home here.

Chapter 1 – Introduction

Proteins are held together in characteristic folded structures by a multitude of weak, competing interactions. Considerable research effort has been dedicated to quantifying these interactions and their relative importance in the hope that such studies would yield an improved predictive understanding of protein folding and structure. The difficulty of this task is heightened by the context-dependent nature of these interactions, which has motivated the development of simpler model systems of protein structure. One of the most important such systems, and the subject of this dissertation, is the isolated alpha helix.

Alpha helices, in which backbone carbonyl oxygen atoms form hydrogen bonds with backbone amide hydrogen atoms of residues four positions subsequent, comprise nearly 30% of globular protein structure[1]. Most naturally occurring alpha helices are stabilized by tertiary interactions and will not fold outside the context of the protein[2]. However, some amino acid sequences, particularly those with an abundance of alanine residues, exhibit unusually high helicity, even when relatively short and lacking stabilizing side-chain interactions[3]. By the end of the 1980s, it was clear that, depending on the amino acid sequence, some short peptides could show isolated helix formation. With the advent of commercial peptide synthesizers, it became possible to chemically synthesize alanine-based peptides that varied in sequence and length and to evaluate their helicity using circular dichroism. These studies led to a revised understanding of the helical propensities of each amino acid and experimental confirmation of an equilibrium model of the helix-coil transition[4].

This equilibrium model of the helix-coil transition treats each individual amino acid as being in one of two states, a helical state or an unstructured, random coil state[5]. The energetic cost of forming a helical segment of a given length comprises a nucleation penalty associated with forming the first turn of the helix multiplied by residue-specific elongation terms based on the relative preference of each additional amino acid for the helical state. Much of the nucleation penalty is associated with the chain entropy lost in forming the first hydrogen-bonded turn of an otherwise random coil. Elongation is also opposed by loss of chain entropy but is favored by a loss of enthalpy from hydrogen bond formation. Because the entropy lost depends heavily on the structure of the side chain, elongation terms may be favorable or unfavorable depending of the identity of the amino acid. The high cost of nucleation coupled with relatively little favorable energy due to elongation makes short helices unlikely, granting cooperativity to the helix-coil transition[4]. The high nucleation cost also means it is unlikely that a polypeptide chain shorter than 100 amino acids would have more than one nucleation site. This latter observation motivates a simple partition function for a polypeptide chain that includes the energetic contributions from the entirely random-coil state and from states comprising every possible helix length and position along a chain. The average helicity of an individual residue can be calculated from the fraction of those weighted states in which the residue falls within the helical window. The average helicity of the chain, which is usually the property measured in bulk spectroscopic experiments, is simply the average of the helicity for each residue[5].

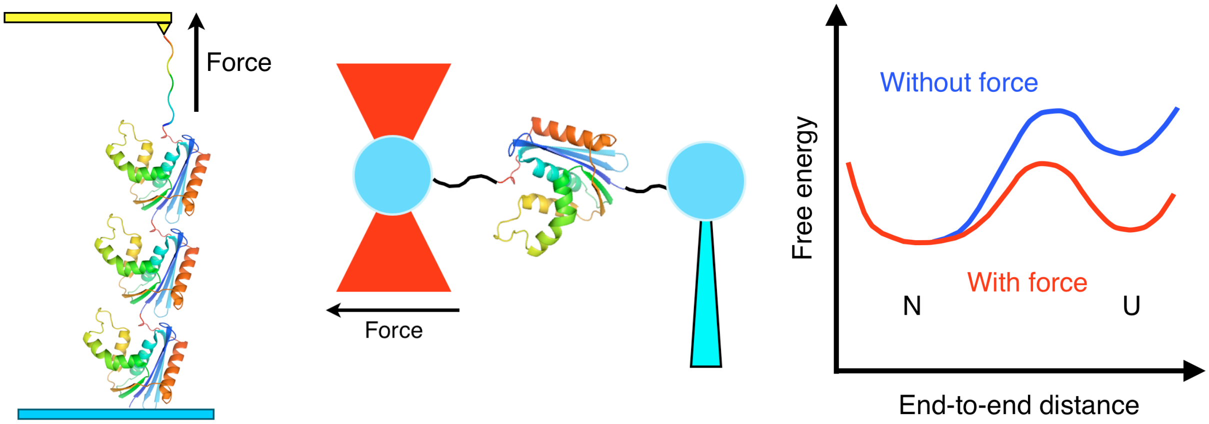

Figure 1. Two approaches for applying force to proteins: an atomic force microscope (left) and an optical tweezers (center). Force has the effect of biasing the folding free energy landscape proportionally to total change in end-to-end extension between the native and unfolded states.

This model of the helix-coil transition has been augmented with empirical data to capture sequence-dependence, longer-range side chain interactions, and the effects of temperature and pH[6]. One important perturbant it does not capture, however, is mechanical force. Mechanical force is increasingly recognized as a factor in many biological processes, including membrane fusion, protein translocation, protein degradation, cellular transport, and movement[7]. Alpha helices take part in most of these processes indirectly, as elements of protein structure, and are known to play a direct role in a few. The alpha helical arms of myosin VI, for example, act as force transducers, while the folding and assembly of SNARE proteins into coiled-coils drives membrane fusion[8,9]. Thus, understanding how alpha helices respond to mechanical force will further our mechanistic understanding of the processes in which they take part.

Awareness of the role played by mechanical force in biology has been driven by the development of single-molecule force spectroscopy. Using the techniques of atomic force spectroscopy (AFM) and optical tweezers, researchers can apply picoNewton scale forces to individual biomolecules, including nucleic acids and proteins, and measure nanometer extensions corresponding to unfolding (Fig. 1, left and center)[10-12]. Force biases molecules to more extended states in a well defined manner, effecting a change in free energy equal to the product of the applied force and the difference in extension between the two states[13]: $\Delta G = \Delta G^{\circ} - F\Delta x$ (Fig. 1, right). This property makes it possible to determine the thermodynamic stability of a single molecule by applying a range of forces and measuring the equilibrium constants between the compact, folded state and the extended, unfolded state, akin to an equilibrium melt using temperature or chemical denaturant frequently used in ensemble-based studies.

Force spectroscopy can also yield kinetic information. In an ideal situation, the applied force creates a situation where the two conformations are close in energy, with an equilibrium constant near unity, and the molecule spontaneously transitions between the two nearly isoenergetic states. If the transition rate at this force is within the practical timeframe of the experimental detection, the molecule will appear to hop between the two states. The average lifetime in each state corresponds to the inverse of the

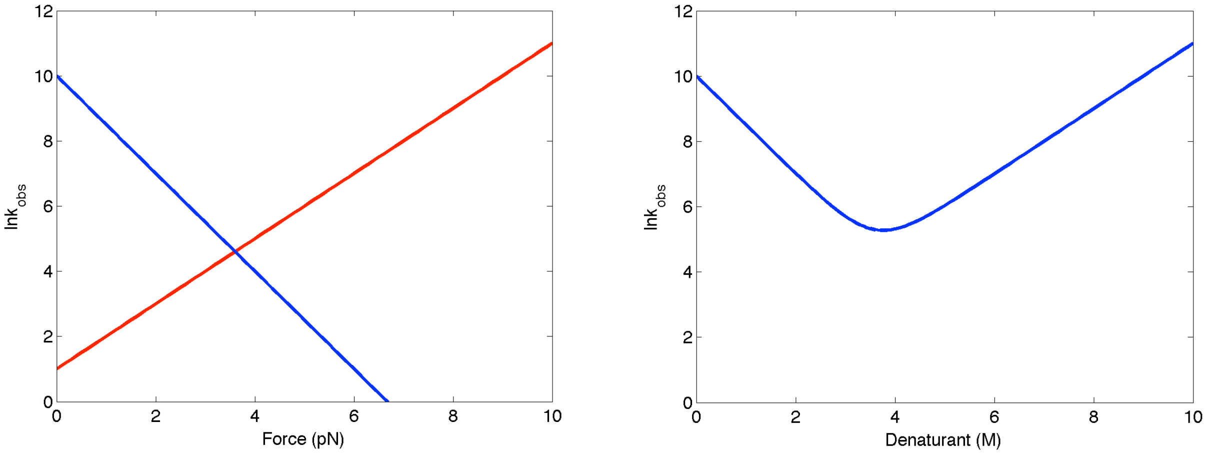

Figure 2. Plotting the effect of force on the rate of folding (left, blue) and unfolding (red) produces a chevron analogous to that observed in bulk kinetic experiments with denaturant that show only the sum of both rates (right).

transition rate out of that state. Because these lifetimes are exponentially distributed, the transition rate may also be fit accordingly[14]. However, many proteins do not exhibit this hopping behavior within the experimentally accessible timescales. For these cases, kinetics may be determined by separately measuring folding and unfolding rates. In one experimental mode, called force jump, a force is instantaneously applied that induces folding or unfolding on a measurable timescale, akin to a stopped-flow experiment. Transition rates can be calculated from the average time the molecule spends in the initial state before a transition. In another experimental mode, called force ramp, the applied force is constantly increasing. This yields a distribution of unfolding forces that will depend on the specific loading rate, defined as force applied per unit time, which is typically held constant. Since in a simple two-state transition the logarithms of both the unfolding and refolding rates show a linear dependence on force, plotting them produces a chevron analogous to that used to analyze denaturant-dependent kinetics[15,16](Fig. 2).

To date, about a dozen model proteins have been studied using this approach. These studies have yielded several important insights. First, proteins exhibit wide variation in mechanical stability. Many, but not all, unfold in the 0.5-65 pN range accessible to optical tweezers experiments[17]. Second, the direction of force application makes a difference, indicating that the folding and unfolding pathways are not always identical to those in the absence of force[15,18-21]. Third, the unfolding transitions for most proteins yield the entire expected contour length, suggesting that there is no residual structure in these mechanical unfolding experiments[10,11,15,22]. Fourth, we do not yet have the ability to predict the mechanical stability of an individual protein[23]. Much remains unknown about the effect of force of the energy landscape of a protein.

In both AFM and optical tweezers experiments, mechanical unfolding is achieved by tethering the molecule of interest between two solid supports and then moving those supports apart. Because a known spring constant relates the position of the supports to the force they apply, measuring their position allows molecular extension and applied force to be simultaneously monitored. In the optical tweezers, the supports are micron-sized beads, while in the AFM they are a coverslip and a cantilever. Both approaches require a large distance between the supports. This can be accomplished by studying naturally polymeric proteins, such as the muscle protein titin[12], or by generating genes encoding synthetic polymeric proteins[24]. Yang, *et al.*, generated polymers of phage T4 lysozyme by introducing cysteine residues predicted to form intermolecular contacts based on the crystal structure and then oxidizing the protein in the resulting crystals[25]. In 2005, Bustamante and Marqusee and coworkers developed a general approach for studying small globular proteins by conjugating long pieces of DNA called handles to precise points in the protein[10,26]. While initial mechanical unfolding studies primarily used AFM, the optical tweezers has become the instrument of choice over the last two decades.

The optical tweezers approach was first applied to the muscle protein titin, which established basic features of pulling trajectories, including independent mechanical unfolding of individual domains, hysteresis in refolding, and worm-like chain (WLC) behavior of unfolded polypeptides[27,28]. A follow-up study using a two-bead optical tweezers assay to investigate components of titin in isolation, including individual immuglobulin segments and the PEVK region, demonstrated that titin's elasticity arises from these components acting in series and that the persistence length of the PEVK component varies with ionic strength and temperature, suggesting some residual structure in the unfolded state[29]. Marqusee and Bustamante and coworkers used optical tweezers to perturb *E. coli* ribonuclease H and found that over a narrow range of constant applied force, the tethered molecule can be observed to transition between the unfolded state and an intermediate state[10]. Occasionally, the molecule transitioned from this intermediate state to the native state. This conclusively demonstrated that the intermediate is an on-pathway step in folding and represented the first direct observation of three-state folding with optical tweezers. Springer and colleagues mechanically unfolded the A2 domain of von Willebrand factor, the cleavage of which *in vivo* is necessary for proper hemostasis[30]. By comparing the forces required for its unfolding to hydrodynamic forces resulting form arteriolar bleeding, they rationalized that mechanical unfolding of A2 precedes and enables enzymatic cleavage *in vivo*. Follow-up studies demonstrated that calcium stabilizes A2 to mechanical unfolding[31], an effect subsequently shown to arise from a five-fold increase in the refolding rate, suggesting a reversible mechanism for preventing premature unfolding and cleavage[32].

Thanks to these pioneering studies, researchers recognized that optical tweezers were useful not just to determine the effect of force on molecules but to identify new states on the energy landscape that could not be identified with other techniques. Gebhardt, *et al.*, described a determination of the energy landscape of a construct composed of three heptad repeats of the GCN4 leucine zipper[33]. In addition to the native and unfolded states, two equilibrium intermediates corresponding to structures with partially folded repeats are identified using constant force experiments. When Zhang and coworkers subsequently examined a construct composed of a single GCN4 domain, they observed two-state folding[19]. This work laid the foundation for later studies of the GCN4 variants pIL and pER, which were shown to exhibit dynamic registry, effectively sliding between different misfolded states[34]. Shank, *et al.*, compared the folding cooperativity of the phage T4 lysozyme with its circular permutant[11]. By changing the handle attachment positions, force could be specifically applied to either of lysozyme's two subdomains. With the folding signatures for each subdomain thus established, it was shown that the native protein folded cooperatively while the circular permutant exhibited independent folding of the C-domain. This motivated the supposition that evolution may select for topologies enforcing cooperative folding in order to avoid kinetic trapping and misfolding. This study was also notable for its use of the Crooks' fluctuation theorem to extract equilibrium folding free energies from nonequilibrium mechanical unfolding measurements. Lindquist and colleagues used self-templating yeast prion protein to assemble fibrils that could be manipulated with an optical trap and observed unfolding and rupture and forces above 250 pN[35]. In a landmark study, Rief and coworkers identified four different populated equilibrium intermediate states in the folding of calmodulin, two of which were off-pathway[22]. Some states, due to similar lengths, could only be discerned from each other by their dissimilar transition rates.

Eventually, longstanding questions in the protein-folding field were addressed with optical tweezers. Kaiser, *et al.*, demonstrated that T4 lysozyme folds more slowly when tethered close to the ribosome[36]. Elms, *et al.*, found that apomyoglobin in a pH-induced molten globule state exhibits broad deformability across two different pulling axes, which could be a general property of molten globules[15]. Cecconi and colleagues, however, showed that the native state of ACBP was even more compliant, despite having high contact order and a native fold, and suggested that its high helix propensity could be responsible[37]. Woodside and colleagues applied the optical tweezers technique to prion protein[38]. Contrary to expectations, no partially folded states through which amyloid fibers might form were seen on the native folding pathway. Instead, three different misfolding pathways were observed that are favored over native folding. Mutant prions that are more prone to aggregation exhibit higher occupancy in these misfolded pathways, suggesting their likely role in the mechanism of infection. Gao, *et al.*, found that SNARE proteins, whose folding and assembly drive membrane fusion, exhibit a half-zippered intermediate that rapidly and forcefully transitions to the folded state, delivering enough energy to mediate fusion[39]. Jagannathan, *et al.*, mechanically unfolded src SH3 using two different pulling geometries and observed that unfolding with a shearing geometry follows different pathways under low and high force application[21]. Tans and colleagues showed that trigger factor promotes native folding of maltose binding protein by comparing folding intermediates in its presence and absence[40]. This result demonstrates that chaperones may directly alter the energy landscape of single proteins and are not limited to suppressing aggregation and rescuing misfolded states.

As optical-tweezers technology improved, with better resolution and faster detectors, previously intractable systems became amenable. Zoldak, *et al.*, describes the application of a novel optical-tweezers technique enabling microsecond sampling to the folding of villin headpiece[41]. This is a significant development because it brings the timescales accessible to single molecule techniques closer to those accessible to molecular dynamics simulations. Rognoni, *et al.*, pulled on the force-sensing domain of human filamin and demonstrated that the configuration of its proline switch determined its unfolding force and thus played an important role in its function[42]. Zorman, *et al.*, compared neuronal, GLUT4, endosomal, and yeast SNARE proteins and found that despite sharing intermediates and kinetics, the four SNARE proteins differ in their energetics, suggesting a regulatory mechanism[43]. Cecconi and colleagues pulled on human neuronal calcium sensor-1, a protein involved in neurotransmitter release and implicated in a number of neurological diseases, and found that pathologically high calcium concentrations slow productive folding, suggesting a link between calcium dysregulation and neurodegeneration[44]. Guinn, *et al.*, incorporated chemical denaturants and mutational analysis into an optical tweezers setup to demonstrate that src SH3 can unfold via multiple pathways with distinct transition states[45].

Clearly, the last decade has been very fruitful for our understanding of the mechanical stability of globular proteins. In spite of this, the effect of force on a basic unit of secondary structure, the alpha helix, has remained elusive. There have been two notable attempts to measure this, both using AFM. Afrin, *et al.*, reported that a helical alanine peptide exhibits force-extension behavior similar to unstructured polypeptide, suggesting that unfolding of the helix occurs below the nanoNewton forces probed in their experiment[46]. Berkemeier, *et al.*, applied force across the helical linker that connects and packs onto the My12 and My13 immunoglobulin domains of myomesin[47]. The coupled detachment and unfolding of this linker occurs at roughly 30 pN, placing a likely upper bound of the force for isolated helix unfolding.

There are several reasons why the effect of force on an isolated helix is difficult to experimentally capture. First, the helix-coil transition is not two-state but is instead a rapid equilibrium comprising many partially helical states[5,48]; any measurement will likely represent an equilibrium average of helical content that decreases continuously with force. This continuous behavior may be difficult to discern from the force-extension response associated with the unfolded polypeptide and the DNA handles. Second, the force or force range over which this transition occurs is not known. The observation that proteins unfold to their contour lengths in mechanical unfolding experiments suggests only that helices must unfold at forces lower than or equal to those required to unfold the proteins they constitute. Finally, regardless of the force where the transition occurs, the expected extension change will be very small. For example, assuming the unfolded coil state is an inextensible worm-like chain with a persistence length of 6.5 Å[49], the expected extension change per residue would range from zero at 4.9 pN to ~1.5 Å at 50 pN. As helices in proteins contain 12 residues on average[50,51], this represents an extension change on the order of 1 nm, approaching the detection limit for conventional force spectroscopic techniques. Considering these factors, understanding the effect of force on the alpha helix and the helix-coil transition requires development of a new approach.

In this dissertation I develop a hybrid magnetic tweezers-single molecule FRET (smFRET) assay with novel labeling methodology to characterize the effect of force on the helix-coil transition. I hypothesized that smFRET would provide a measure of extension sensitive enough to detect changes in helical content. Chapter two describes the design of a novel hybrid microscope incorporating smFRET and magnetic tweezers. Chapter three details the chemical synthesis and functionalization of proteins for study in this instrument. Chapter four discusses the calibration of this instrument. Finally, chapter five presents the results from and interpretation of the effect of force on the helix-coil transition.

Chapter 2 – Development of a hybrid smFRET-magnetic tweezers instrument

The experimental setup implemented for this dissertation research is derived from an objective-total internal reflection fluorescence (TIRF) smFRET microscope that has been augmented with magnetic tweezers. While both techniques are well established in the literature, discussion of the novel developments in the hybrid instrument requires an initial overview of both techniques. Specific components used in the hybrid instrument will be highlighted as they arise.

TIRF microscopy exploits a sharply decaying evanescent field to excite fluorophores tethered to a surface without significantly penetrating the solution, resulting in high signal-to-noise that enables the detection of single molecules[52]. This evanescent field is produced when light incident on an interface of higher refractive index into lower refractive index strikes at such an oblique angle that Snell's law predicts an angle of reflection greater than ninety degrees. In such cases, the light is totally internally reflected. For the interface between glass, which nominally has a refractive index of 1.51, and water or buffer, which nominally has a refractive index of 1.33, the critical angle beyond which total internal reflection is observed is 61.7°. The coherent light of a laser can generate an evanescent field as wide as the incident beam. Rather than align a laser so that it strikes an interface above the critical angle, the evanescent field is typically produced using one of two methods. In the first, called prism TIRF, the excitation laser light strikes the angled side of a prism mounted on a microscope slide. The air-glass interface refracts the light so that it strikes the glass-water interface above the critical angle. In the second method, called objective TIRF, excitation light is directed into the back of the microscope objective. For objectives with sufficiently high numerical aperture, the excitation laser light will be refracted by the objective itself to such an angle that it will be beyond the critical angle when it reaches the glass-water interface. Each approach has its own advantages and disadvantages, and both are widely used. However, only objective TIRF is amenable to experiments incorporating magnetic tweezers.

Prism TIRF is incompatible with magnetic tweezers for reasons of geometry. In both TIRF configurations, fluorescent molecules in aqueous buffer are deposited within a microfluidic chamber made from a microscope slide and a coverslip, which faces the objective. In prism TIRF, the evanescent field is generated on the inner surface of the microscope slide, and consequently, the imaged molecules are mounted on the inner surface of the microscope slide as well. Were force to be applied to a molecule tethered on the surface, it would have to direct it towards the objective and the rest of the microscope. Magnetic tweezers function, however, by directing paramagnetic spheres towards regions of higher magnetic field gradient, which are sharpest directly between magnetic poles. In order to employ a hybrid prism TIRF-magnetic tweezers, the magnet would need to physically occupy the same space as, or be incorporated into, the objective itself.

Hybrid objective TIRF-magnetic tweezers are consequently much more practical. In objective TIRF, the evanescent field is generated on the inner surface of the coverslip, which dictates that the imaged molecules be tethered there as well. The application of force on a tethered molecule away from the surface now requires a

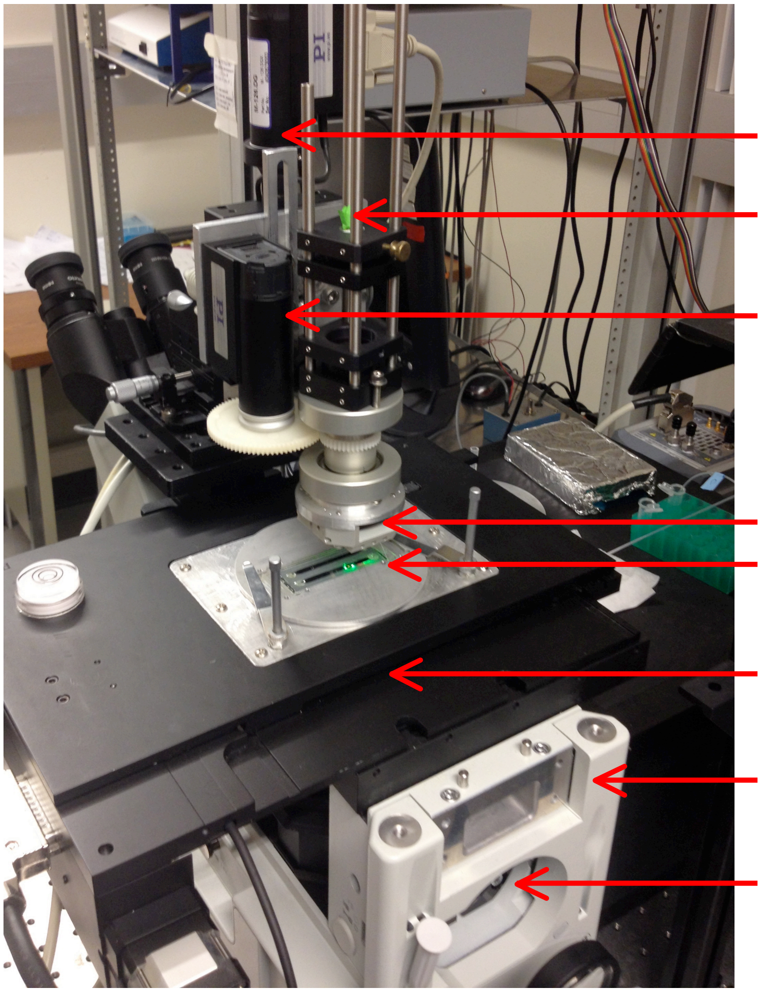

Figure 3. A photo of the instrument showing how simultaneous force application and TIRF are achieved.

magnet be placed opposite the objective, on the other side of the microscope slide. This is the approach used (Fig. 3). Like many commercial fluorescent microscopes, the Olympus IX71 used here is of the inverted variety, with the objective facing up, so the microfluidic chamber rests on the stage with the coverslip facing down, and the magnet is mounted above.

Objective TIRF has a fundamental requirement: an objective of high numerical aperture (NA). Although TIRF is theoretically possible with an objective having an NA only slightly greater than the medium of the sample, only a small region of the visible field will be excited. Better illumination is achieved with higher NA objectives, which also provide better resolving power at high magnification, crucial characteristics for imaging single molecules. For these reasons, the hybrid instrument employs an Olympus UPlanSApo 100x/1.4NA oil-immersion objective. High magnification and oil-immersion are not typical characteristics of magnetic tweezers, and their ramifications will be revisited later.

In order to generate an evanescent wave through TIR, the excitation laser must enter the back of the objective far enough from its center axis so that the objective refracts it beyond the critical angle. If the laser is aligned with or near the center axis, the beam will be normally incident or refracted on the glass-water interface, as in

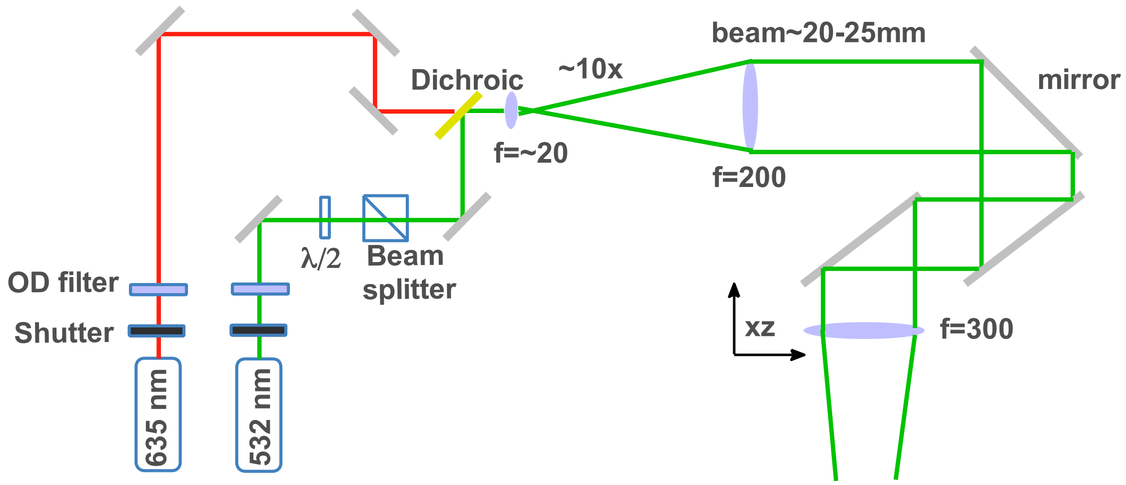

Figure 4. Diagram of excitation optics. The primary excitation beam must be expanded to overfill the back entrance port of the microscope. A second polarizing beam splitter directly after the neutral density filter, as well as a quarter wave plate positioned before the beam expander, are not shown.

epifluorescence. The farther the laser enters from the center axis, the larger the incident angle on the interface, until the maximum angle permitted by the objective is reached. Any father from center, and the laser will not even enter the objective. In principle, every position on the circle with the same distance from the center will produce the same incident angle. Because of this, the hybrid instrument is aligned with the beam entering left of the center of the back entrance port of the microscope, and a single translation stage controls how far to the left, allowing adjustment to every possible incident angle. The left side is chosen for safety reasons; if the incident angle is adjusted out of the range of TIR, the laser is refracted onto a wall on the right, rather than onto the user.

The focusing power of the objective means that the excitation laser must completely fill the back of the objective in order to excite the entire field of view. This is achieved in the hybrid instrument through the use of a two-lens telescope referred to as a beam expander, which enlarges the beam diameter from roughly 2.5 mm to 2.5 cm (Fig. 4). The expanded diameter must be slightly larger than the diameter of the back-entry port of the microscope to account for the beam entering slightly left of center. An equal diameter would leave a crescent on the right side of the field of view dark. When sufficiently expanded, a crescent of rejected excitation light will be visible along the left side of the entrance port.

There are two excitation sources on the hybrid instrument, a green solid state CrystaLaser laser at 532 nm with a nominal power of 75 mW and a red HeNe Thorlabs laser at 635 nm with a nominal power of 18 mW. The green laser is primarily used for FRET, while the red may be used to directly excite acceptor fluorophores. Both are mounted using standard 1/4” hardware at a height of 18.5 cm above a Newport self-correcting optical table, the same height as the back entry port of the microscope. Directly in front of each laser is a Uniblitz shutter, followed by tandem filter wheels filled with various neutral density filters. These may be used for a coarse adjustment of laser power, for example, to perform initial alignments of the green laser at powers lower than 5 mW, the threshold for safe unprotected human viewing.

Lasers are typically linearly polarized, up-and-down in the direction that they are mounted. The green laser on the hybrid instrument, contrary to manufacturer specifications, is elliptically polarized. Tests using a polarization beam splitter in a rotating mount and a power meter have been used to verify that there exists no angle at which more than roughly three-quarters of the light passes through. To clean this polarization, a polarizing beam splitter is mounted directly in front of the filter wheels. The reflected component, approximately one quarter of the total laser power, is directed into an optical beam dump, while the transmitted light is retained. This linearized light passes through a half-lambda waveplate mounted in a rotary mount. Rotating the half-lambda waveplate rotates the linear polarization of the beam going into another polarization beam splitter. This splitter directs reflected light into another beam dump. Thus, rotating the waveplate allows fine adjustment of the laser power. As the polarization of the incident beam is rotated, more light is rejected by the subsequent beam splitter, lowering the power of the transmitted beam used for excitation.

In order to provide uniform excitation, this linearly polarized transmitted excitation beam must be circularly polarized. This is accomplished through a quarter waveplate placed next along the optical axis, aligned with the strong axis 45° from the linear polarization that enters it. The polarization of the beam used the create evanescent field is important for the hybrid instrument, because it cannot be stated with certainty that the fluorophores bound to a molecule will rotate freely when that molecule is pulled in one direction, away from the surface. This is still an important consideration in the absence of force when the free rotation of fluorophores might be constrained by proximity to the surface.

The quarter waveplate is mounted on the same cage system as the beam-expanding telescope. This is one of two points, the other being the entrance to the microscope, where the exact position and angle of the incident beam must be precisely aligned. As such, two tip-tilt mirrors are present at both these positions. Alignment is straightforward using an optical target.

When the left-of-center, expanded excitation beam finally enters the back of the microscope, it strikes a polychroic mirror that reflects it up through the objective. This mirror must reflect the 532 nm green and 635 nm red excitation light, but allow fluorescence from green fluorophores and red fluorophores to pass through. It must also permit the near-infrared light used in the autofocus system, discussed later, to be transmitted. As with all fluorescence techniques, a Stokes' shift between excitation and emission light allows scattered excitation light, which is of much greater intensity than fluorescent light, to be rejected by dichroic mirrors. The hybrid instrument uses a Semrock quad-band Di01-R405/488/532/635 polychroic filter.

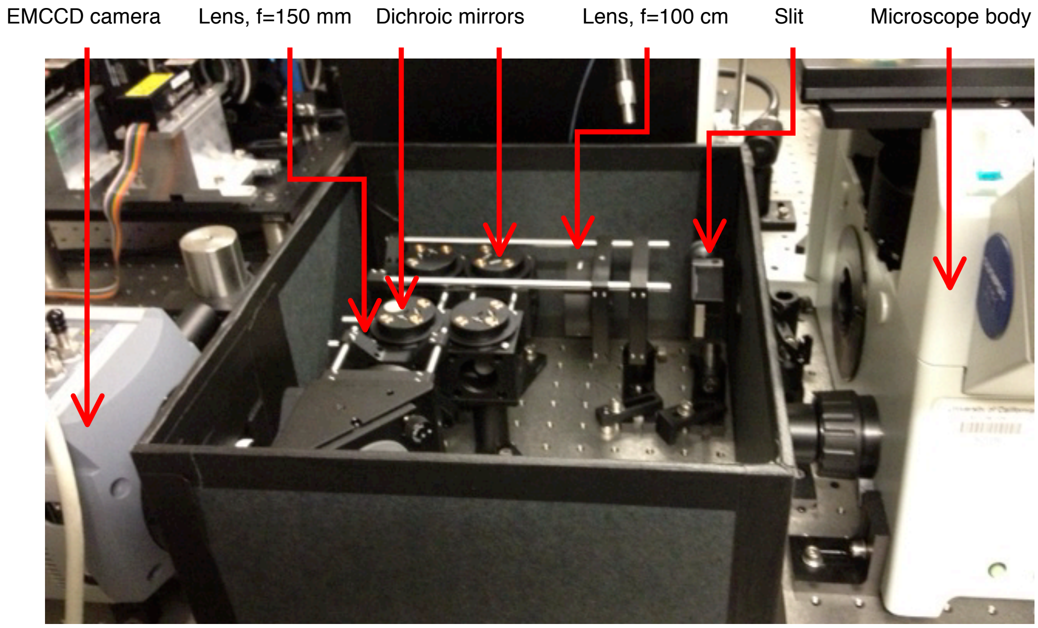

Figure 5. Photo of emission optics. Independently adjustable mirrors and dichroic mirrors spatially separate donor and acceptor fluorescence onto an EMCCD camera.

The emission optics must spatially separate filtered green fluorescence from red fluorescence and direct the parallel channels onto the EMCCD detector. Fluorescent light from the fluorophores, as well as a tiny fraction of excitation light not reflected by the polychroic mirror, passes through the polychroic mirror in the filter cube to the bottom of the microscope. Here, a mirror directs the light either to the oculars, or to the emission optics and camera to the left of the microscope. It is important eye protection be used if the oculars are to be used, as potentially significant excitation light will be captured.

Emitted light leaving the microscope passes first through an autofocus system, to be discussed later, and then through a rectangular slit (Fig. 5). The purpose of this slit is to create a field of view with straight edges, so that donor and acceptor channels may be displayed side-by-side without overlap. The truncated light then passes through a homemade dual-view system, which consists of two mirrors and two dichroic mirrors. The first dichroic mirror transmits light from acceptor fluorophores and reflects light from donor fluorophores onto two independently adjustable mirrors. These mirrors are used to align the donor channel to the left of the acceptor channel. The second dichroic mirror recombines the two fluorescent channels before the detector. A 1.5x telescope consisting of two lenses, one placed before the dual-view, one after, is used to magnify the image onto the camera.

The Andor iXon+ camera has a number of features that make it suited for single molecule fluorescence. It particular, it incorporates an electron multiplying charge-coupled device that permits detection of the small numbers of photons emitted by single fluorophores. It also incorporates a frame transfer feature, which increases the fraction of time it can collect photons. Instead of performing the digital readout of charge directly from the exposed CCD, the charge is first transferred to a secondary CCD and the exposed CCD detector is subsequently cleared. This frees up the exposed detector to resume collecting light rather than waiting for each frame to be read out. This process enables full 512x512 pixel movies to be read out at a rate of 32.949 Hz with an exposure time of 0.03035 s. Using sub-images, binning, and isolated crop mode can further increase this rate. Vertical readout is much slower than horizontal readout, so the number of vertical lines in a subimage has the largest effect on this rate. For a subimage of a given height, there is a slight dependence of readout rate on vertical position.

The autofocus system works by exploiting Fresnel's laws of reflectance. An LED at 780 nm is directed into the side exit port of the microscope up through the objective and reflects off the glass-water interface on the inside of the coverslip. This reflected light strikes a detector within the autofocus unit. Critically, the amount of light reflected, rather than transmitted, depends on the distance between the objective and the glass-water interface. Thus, the intensity of the reflected light as a function of this distance can be used to create a calibration curve centered around the position where surface fluorophores are in focus. Whenever the system moves out of focus, the reflected intensity is fed back through a piezo actuator controlling the height of the objective.

In a magnetic tweezers, a permanent magnet or electromagnet exerts a force on a molecularly-bound paramagnetic microsphere proportional to the magnet's magnetic field gradient, the volume of paramagnetic material, and the polarization of the microsphere[53]. The molecule is tethered to the surface of a coverslip or a flow cell on one end and to the magnetic microsphere, often called a bead, at the other. The magnetic force applied typically pulls the bead away from the surface and the coverslip. Tracking of the position of the microsphere is carried out by a camera. In order to determine the height of the bead above the surface, a method has been developed that exploits the change in diffraction rings as a bead moves out of focus[54]. A lookup table for bead height is made by imaging a fixed bead at constant intervals (e.g. 100 μm or 200 μm). The center of the bead is identified by finding the position which exhibits the best four-fold symmetry and then the intensity profile as a function of radius for each known defocused position is measured[55]. This is used to fit a polynomial that relates the intensity profile with defocus. In a typical experiment, both a tethered bead and fixed, reference bead are present within the field of view. Both are out-of-focus, usually with the focus beyond both. The position and height of the reference bead are calculated over time to correct for drift in the position of the tethered bead.

One crucial development employed the hybrid instrument is the use of surface-bound fluorophores, rather than immobilized beads, as the fiducial reference. In a magnetic tweezers, the field of view is large enough to accommodate many beads. The high magnification required for single fluorophore imaging, however, means that fewer beads can be present in the same field of view without interacting (e.g. sticking together due to magnetic attraction) or having their diffraction rings overlap. Furthermore, in magnetic tweezers experiments, beads are deposited on the surface prior to passivation with bovine serum albumin. Single-molecule fluorescence, on the other hand, requires a more stringent passivation involving treatment of coverslips with potassium hydroxide, aminosilane and PEG, which would strip any beads immobilized beforehand and render subsequent immobilization difficult.

Magnetic tweezers, and the camera-based detection they rely on, face a trade off between multiplexing and frame rate. The smaller the image, in pixels, the faster the readout, so an image of a single bead can necessarily be read out faster than an image that includes a reference bead as well. Because tethered and reference beads are deposited randomly, it is very likely that no reference bead will be present with the same field of view.

The construction of the microfluidic chamber used in experiments on the hybrid instrument incorporates eclectic design elements and improvements arising from many revisions to satisfy the requirements of both single molecule fluorescence imaging and force spectroscopy. From the standpoint of fluorescence imaging, the primary requirement is that the imaged surface on the inside of the coverslip exhibits low background. In practice, this means that coverslips must be exceptionally clean. Any particulates that adhere to or settle on the surface are liable to elastically scatter light, resulting in the appearance of surface artifacts that can obscure or be mistaken for fluorophores. A secondary requirement of the chamber is that only the molecule of interest is able to bind to the surface and only in a particular way that prevents direct interaction with the surface. Many biomolecules, including those intentionally introduced into the chamber, may directly adhere to the glass surface, producing background artifacts that cleaning was supposed to eliminate. Furthermore, interactions with the hydrophilic surface may cause nonspecifically adsorbed molecules of interest to change their conformation or behavior, compromising the validity of observations of them.

The acknowledged solution to both these requirements is to chemically clean and passivate the slide and coverslip used to make the microfluidic chamber. Roy, *et al.*, describes a commonly used method, which is adapted here[52]. Cleaning is performed by successive rounds of sonication in the presence of detergent, solvent, and strong base. Passivation is carried out by silanizing the cleaned glass and treating it with a mixture of PEG-NHS-ester and small amounts of Biotin-PEG-NHS-ester. The surface is thus rendered hydrophobic and the molecule of interest is specifically attached through the biotin moiety.

Two important simplifications may be made to this method by recognizing that it was developed for employment with the prism-TIRF instruments used in TJ Ha's lab. In prism-TIRF, because the excitation laser passes through the slide, better, more uniform TIRF is achieved by using slides made of quartz. Given their high cost, these slides are reused. Since the slide is also the imaged surface in prism-TIRF, the cleaning regimen must be especially stringent. Used slides will be covered not just in fluorophores from previous experiments, but also in the stubborn adhesives present in the tape and epoxy used to make their chamber. On the other hand, with the objective-TIRF configuration of the hybrid instrument, the slide carries much less importance. Because it does not act as a laser medium, it can be made of single-use glass that doesn't require as much cleaning, and because no imaging happens through it, it need not even be passivated. This minimizes the time and reagents expended for cleaning slides and effectively doubles the number of usable surfaces that may be passivated with a batch of PEG.

This cleaning and passivation scheme goes far beyond that used in a typical magnetic tweezers or optical tweezers experiment, and scientists from a force spectroscopy background may wonder to what extent it is truly necessary. Clean glass is not nearly as crucial for tweezers experiments and may be used out-of-the-box, without any cleaning at all, or cursorily sprayed with methanol and dried with nitrogen or a Kim-wipe. Any absorbance or scattering of light by surface particulates will be inconsequential compared with the intensities of light used for bright-field imaging and optical trapping. Furthermore, in tweezers' experiments the focal plane is typically far from any surface and contaminants bound thereon. Neither condition holds when imaging single fluorophores on a surface. The light emitted by a single fluorophore will often be of comparable intensity to that scattered by a contaminating particle on the surface and may exhibit a very similar profile. In order to clearly identify and characterize true fluorophores, it is thus very important that the glass be clean.

Passivation is also less crucial in tweezers experiments than in single-molecule fluorescence, largely because it serves a fundamentally different purpose. In a magnetic tweezers experiment, for example, the primary purpose of passivation is to enhance yield by preventing magnetic beads and nucleic acids tethers from nonspecifically attaching to the surface. Without passivation, diffraction rings from surface-bound beads would interfere with the detection of tethered beads and nucleic acids tethers might form weak surface attachments that broke under applied force. Both effects would be obvious and self-mitigating: observations would be made only on isolated tethers that could withstand sufficient applied force. Yet passivation isn't crucial, as illustrated by optical tweezers experiments, which don't use it at all. There, the process of trapping single beads and fishing promotes the selection specifically attached tethers. A trapped bead non-specifically attached to another will be discarded, while a nonspecific tether attachment will be broken and reformed during fishing before any data is taken on it.

In TIRF single-molecule fluorescence, passivation serves a very different purpose. The molecule of interest must be tethered close to the surface, but ideally, not in a manner that allows it to interact with the surface, as this could change the conformation or behavior of the molecule. However, both nucleic acids and proteins will readily adsorb onto a glass surface and may exhibit no obvious discernible difference from those tethered as intended. As a consequence, there will be no way to exclude observations from these nonspecific tethers, as in the tweezers case. Thus, passivation is crucial here, not just to preserve the low level of background, but to ensure that any observed molecular behavior does not arise from artifactual surface interactions.

A counterargument against passivation may be raised that the situation of the hybrid instrument is more akin to that of a magnetic tweezers, where nonspecific tethers will be broken by the application of force and thus contribute no spurious data. It is true that, unlike in the case of a typical single-molecule fluorescence experiment, observations will only come from molecules bound through DNA to magnetic beads that withstand the application of forces of 30 pN. This will likely preferentially select for specifically bound molecules. It is also true that initial experiments using DNA hairpins were successfully conducted using the BSA passivation scheme commonly used in magnetic tweezers experiments. However, the relevant similarities between the two experiments end here. Experiments in the hybrid instrument involve an uncharacterized protein positioned close to the surface, and an adsorptive interaction between the two could completely alter the observed behavior. Magnetic tweezers experiments typically involve only nucleic acid near the surface, as part of a much longer tether. Nucleic acid is less prone to adsorption, and any nonspecific interaction between it and the surface would merely shorten the effective length of the tether, an effect that would be corrected when measuring the height of the bead. Another risk of eschewing passivation in the hybrid instrument is that an interaction between the protein of interest and the surface could be exceptionally strong and withstand the applied force. Even if the application of force perfectly selects only specifically attached tethers, the density of fluorophores on the surface would still be much greater, making isolation of individual molecules more difficult. Finally, adopting a passivation scheme enables conduction of experiments without force. For these reasons, microfluidic chambers used in the hybrid instrument are thoroughly cleaned and passivated.

The next practical design requirement for a microfluidic chamber is that the slide and coverslip are affixed in a way that creates a water-tight cavity for the sample. One of the simplest methods uses parallel pieces of double-sided Scotch tape placed along the length of the coverslip to form a channel. The sample is then introduced via micropipette or syringe directly between the slide and coverslip at one of the ends of this channel. Capillary action will pull the sample through a dry channel, and a Kim-wipe may be used at the other end as a wick to draw additional liquid through. The ends of the channel are then sealed with grease or glue. Roy, *et al.*, describes a slightly modified method: inlet and outlet holes are drilled through the slide before the chamber is assembled, and epoxy is used to seal the ends of each channel. The bottom is cut from a P200 micropipette tip and glued around the inlet, and plastic tubing is glued onto the outlet. The sample is loaded into another P200 micropipette tip and pressed into the tip glued around the inlet, forming a seal. A syringe is then attached to the plastic tubing on the outlet and used to aspirate the sample through the channel. This method has several advantages, namely that sample or activity buffer may be injected while the chamber is mounted on the microscope, that an automated syringe pump may be used, and that negative pressure applies less stress to the coverslip.

The microfluidic chamber construction used for the hybrid instrument makes several improvements upon this design (Fig. 6). First, instead of double-sided Scotch tape, Nescofilm, a paraffin wax film, is used. Nescofilm can be quickly and precisely cut into customized gaskets using a computer-controlled laser cutter. These gaskets, which are also used for making optical tweezers chambers in the Bustamante lab, adhere and seal to glass when heated to 120° C. The only disadvantage of Nescofilm compared to tape is that the PEG passivation considerably diminishes its adhesive capability. To prevent chamber failure and sample leakage, the edges of the coverslip should be reinforced with epoxy. Nescofilm is preferred over Parafilm because it exhibits a broader temperature range between the temperature at which it adheres and the temperature at which it melts. Second, the micropipette tip loaded with sample is pressed and sealed directly into the glass inlet. It is not necessary to use the bottom of another tip as an adapter, perhaps because the inlet holes are drilled with a drill press instead of a hand-

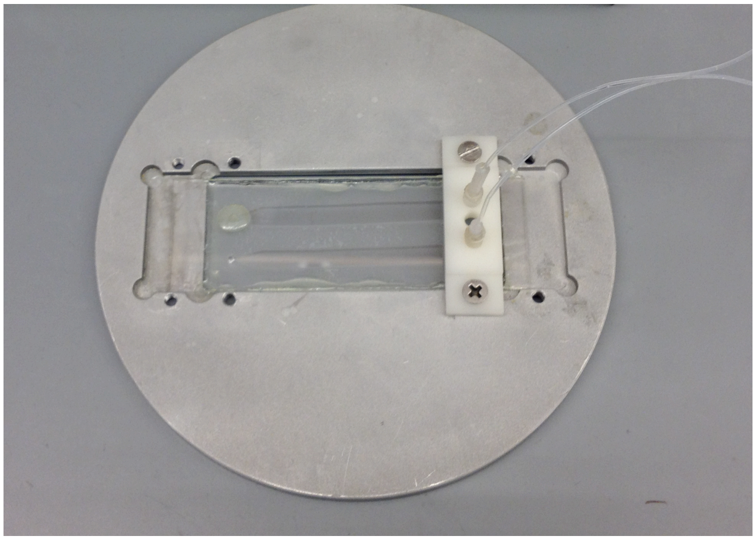

Figure 6. Photo of microfluidic chamber during sample loading. A Delron plastic gasket seals Tygon tubing against the predrilled outlet on the microscope slide. A syringe attached to the other end of the plastic tubing (not shown) pulls sample into the chamber.

held Dremel and are consequently more regular. Finally, instead of gluing the plastic tubing directly to the glass slide for the outlet, a seal is made using Tygon tubing drawn through a Delron gasket. This gasket is screwed down onto the slide during sample loading and can be reused indefinitely.

One additional modification was made to the chamber construction to minimize the possibility of drift due to water, or airflow, a concern especially for magnetic tweezers. Rather than leaving the inlet open to the air above the micropipette tip and the tubing attached to the gasket, both inlet and outlet were sealed with epoxy after sample loading. While this prevents additional sample or activity buffer from being flowed through while mounted on the microscope, this capability was not needed for any of the experiments described in this dissertation. Sealing the inlets and outlets not only minimizes the possibility of drift but confers numerous other advantages as well. Sample evaporation is eliminated and useable sample lifetime is prolonged, with sealed samples even being usable the following day. Potential collisions between the magnet above the chamber and either the inlet pipette tip or outlet tubing are avoided. Furthermore, less oxygen diffuses into sealed channels are fluorophores are observed to be brighter and exhibit longer photobleaching times.

The Nescofilm gasket design currently used has two channels the run the length of the coverslip with roughly a millimeter of material on all sides and between the channels. The channels are tapered at the inlet and outlet to prevent air from being trapped inside. There are three important factors considered in this design. First, the material between channels must be wide enough to prevent leakage between them. Seals between Nescofilm and glass are less likely to be watertight if they are too narrow, and the seal between channels, unlike that at the edge, is not reinforced by epoxy. This problem is more acute with the PEG passivated surface, but rarely occurs with sufficient sealing.

In the preceding discussion it was assumed that the microfluidic chamber would consist of a single coverslip and a microscope slide rather than, for example, the double-coverslip design used for optical tweezers. Why must this be so? Optical tweezers, with their two inward-facing objects, require that both sides be coverslips. Inlets and outlets are etched into one of these coverslips using a laser cutter. Because it has been automated and is computer controlled, this process may be faster than drilling holes in slides, which are too thick to be etched with a laser cutter. Another potential advantage is that a thinner coverslip on top would allow the magnet to descend lower and apply higher forces before colliding with the chamber. Chambers made from two coverslips, however, are considerably more fragile, especially around the inlets and outlets. Those used in the hybrid instrument, unlike those used for optical tweezers, are single-use, and a considerable amount of time and reagents is consumed during the cleaning and passivation process. Additionally, because the chamber must be supported on the instrument, the usable area is decreased when the ends of the coverslip must rest on the stage. For these reasons, the dual-coverslip design, despite its use for optical tweezers, is impractical for the hybrid instrument.

Chapter 3 – Preparation of nucleic acid and protein samples for the hybrid instrument

This chapter will describe the rationale behind the composition of and the steps necessary to synthesize and functionalize experimental samples for study with the hybrid instrument. Two classes of molecule were examined in this dissertation research: DNA hairpins and proteins. While many of the technical challenges involved in functionalizing nucleic acids for hybrid instrument study have already been addressed[56], the successful functionalization of proteins presented here is a novel development. Nevertheless, both molecules will be discussed here, as DNA hairpins are useful systems for confirming instrument calibration, the subject of the next chapter, and because they provide an instructive counterpoint for the difficulties inherent in functionalizing proteins.

Any sample studied with the hybrid instrument must conform to basic requirements imposed by TIRF smFRET and magnetic tweezers. TIRF smFRET requires fluorophores that are bright, due to its single-molecule nature, and photostable, in order to capture molecular trajectories over time. This is typically achieved by conjugating two different small molecule organic fluorophores, or dyes, to the molecule of interest. In order to provide useful information, the distance between these dyes must depend on conformation. TIRF smFRET also requires that samples be tethered to the slide or coverslip surface, within the evanescent field, but in a specific manner that prevents direct interaction that might influence behavior. This requirement is often met by engineering a linkage moiety like biotin into the sample that allows it to attach in a defined way to streptavidin presented on an otherwise passivated surface.

In a magnetic tweezers, a sample must attach specifically to a coverslip on one end and a magnetic bead on the other. Force applied through the magnetic bead should produce some molecular extension that can be monitored by the displacement of the bead. In practice, the attachment chemistry linking the molecule to the surface must be different from that linking it to the bead; otherwise, undesirable scenarios like beads attaching directly to the surface or tandem tethers forming can result. Magnetic tweezer samples also typically incorporate a piece of DNA at least a micron in length, called a handle. This handle serves several purposes: First, it enables visual discernment of beads tethered by a molecule from ones stuck to the surface. Second, it amplifies the signal of Brownian noise used to calculate the applied force. Third, it effectively eliminates nonspecific interactions between the molecule and the surface to which it is tethered. One disadvantage, however, is that long handles limit the response time of the bead, preventing detection of faster molecular transitions. A handle may be generated by PCR or by restriction digest of a plasmid or phage genome. When the molecule of interest is a nucleic acid, it can be incorporated directly or attached via annealing; protein samples require another specific attachment.

Additional considerations arise when these two experimental techniques are combined. Magnetic beads scatter a significant amount of excitation light when within the evanescent field that overwhelms the fluorescence of single fluorophores. To avoid this, the bead must be sufficiently far from the surface. This distance will depend both on the applied force and the penetration depth of the evanescence field. For our setup,

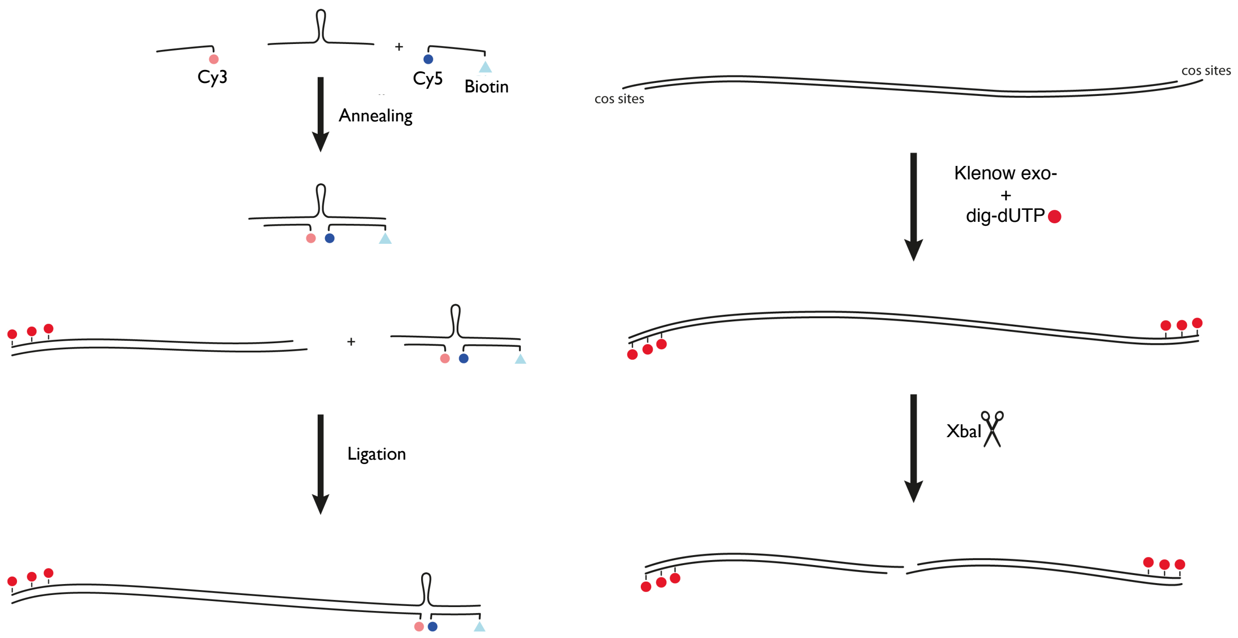

Figure 7. Functionalization scheme for DNA hairpin constructs. Three oligonucleotides are annealed (left) and subsequently ligated to functionalized half-lambda DNA generated as shown (right).

this was not known beforehand. However, because the bead acts only as a force transducer in the hybrid instrument and is not relied upon to report conformational changes, there is no drawback to employing an especially long DNA handle in the sample. Thus, our sample should consist of a molecule of interest that exhibits a force-dependent conformational change and is functionalized with two small-molecule fluorophores whose relative distance depends on this same conformation. It should be tethered to the surface through unique attachment chemistry and a short linker that holds it within the evanescent field while also transducing force and preventing direct interaction. At the site of force application, the system should be conjugated to a long DNA tether of at least a few microns, which in turn should attach to a magnetic bead through a second unique chemistry.

For the DNA hairpin system, this is implemented in the following manner. The DNA hairpin itself is a custom, chemically synthesized oligonucleotide that incorporates a variable loop-forming region in the middle of two constant flanking regions used for annealing to dye-containing oligonucleotides (Fig. 7). Four different loop-forming sequences were chosen from a library previously characterized by Woodside, *et al.*[57] based upon unfolding force and hopping kinetics. Each hairpin oligonucleotide is 5' phosphorylated, begins with the 25 base annealing sequence CTAGCTCATACACTGTACCTGATAG, and ends with the 20 base annealing sequence GCTACCGTAATTGAGACCAC. The 5' annealing sequence begins with CTAG, which will provide an overhang for downstream ligation, but other than that, its sequence is arbitrary. The 3' annealing sequence was chosen to be identical to a thiol-modified oligonucleotide already used in the lab for optical tweezers experiments. A second oligonucleotide with the sequence GTGGTCTCAATTACGGTAGC is synthesized that is completely complementary to the 3' annealing sequence of the hairpin. This oligonucleotide is functionalized with both a 5’ terminal biotin and a Cy5 dye that is incorporated in the phosphate backbone between the second and third nucleotides from the 3’ end. The biotin moiety is used to tether the hairpin to a streptavidin-coated biotin-PEG/PEG passivated surface described in the previous chapter. The Cy5 dye acts as the acceptor fluorophore, and its position above the surface will remain constant regardless of whether the hairpin is open or closed. The dye is placed between backbone phosphate groups rather than at the terminus in order to prevent base-stacking interactions that quench the fluorescence. A third oligonucleotide, CTATCAGGTACAGTGTATGAG, is 3’ phosphorylated and incorporates a Cy3 dye after the fourth nucleotide from the 5’ end. Notably, this oligonucleotide is complementary to the last 21 bases of the 5’ hairpin oligonucleotide annealing sequence. The Cy3 dye, which acts as the donor fluorophore, is also placed in the backbone to prevent base stacking. When the hairpin is closed, the FRET between these fluorophores will be high, and when the hairpin is open, the FRET will be negligible. These three oligonucleotides are resuspended to 100 μM in TE, combined in equimolar amounts, annealed by heating to 90° for 3 minutes, and then slowly cooled to room temperature over an hour in a heat block on the benchtop. Annealing may be monitored using polyacrylamide gel electrophoresis (PAGE) and a Typhoon fluorescence imager. The band representing the complete three-oligonucleotide hairpin dominates the fluorescence intensity of both red and green channels, suggesting a yield above 90%. Two smaller bands representing species lacking one of the two fluorescence oligonucleotides are only faintly visible.

The long DNA handle that joins the hairpin and the magnetic bead is derived from lambda genomic DNA in a multistep process. First, commercially available circular lambda DNA is heated to melt the cohesive ends, called cos sites, and linearize the 48-kbp genome. This leaves a 16-nucleotide overhang at each 5’ end, both of which contain a single adenine nucleotide. It is then treated with exo- Klenow fragment enzyme in the presence of 75 μM digoxigenin-labeled dUTP and 75 μM each unlabeled dATP, dCTP, and dGTP. The labeled DNA is treated with the restriction enzyme XbaI, which cuts at a single T*CTAGA site in half-lambda found at position 24508, producing two similarly sized products roughly 24 kbp and 8.2 μm in length. Both products posses a digoxigenin at one end that binds antidigoxigenin-coated magnetic beads and a 5’ CTAG overhang that is competent for ligation to the overhang on the hairpin sequence. This ligation is carried out with a 4-fold molar excess of hairpin. The ligation process is monitored in the same fashion as annealing. Successful ligation is indicated by complete disappearance of the annealed hairpin band and appearance of a hairpin self-dimer band as well as fluorescence intensity at the half-lambda band position. The fluorescence intensity of this dimer band is roughly ten times that of the half-lambda band, suggesting a strong preference for self-ligation.

The process for functionalizing protein is more involved, as both fluorophores and DNA handles must be attached. This creates a problem because the favored attachment chemistry for both fluorophores and DNA handles has been the cysteine residue, which either acts as a nucleophile with maleimide dyes or forms disulfide bonds with thiol-functionalized DNA. To circumvent this issue, we used two orthogonal chemistries: standard thiol chemistry via cysteine residues and “click” chemistry via the

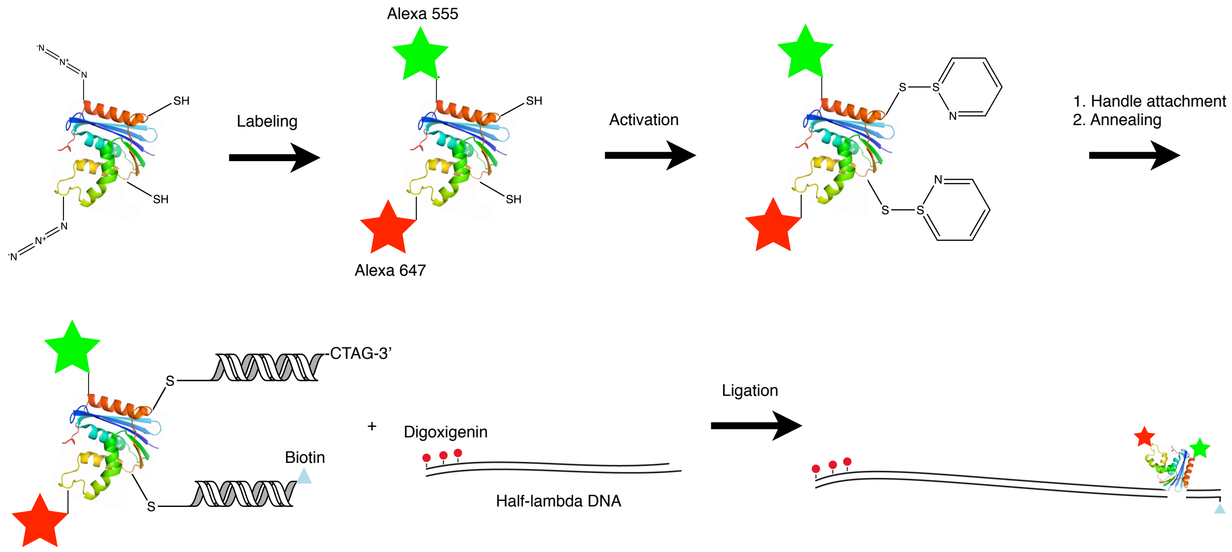

Figure 8. Functionalization scheme for protein constructs. Purified protein is labeled with fluorescent dyes using azide-alkyne chemistry and then activated at cysteine sites with dithiodypridine, which promotes conjugation to a single-stranded thiol-modified DNA oligonucleotide. Subsequent annealing to two different functionalized oligonucleotides produces a species that is ligated to digoxigenin-labeled half-lambda DNA to create the final construct.

unnatural amino acid azidohomoalanine (AHA) that contains an azide group. AHA has been demonstrated to function as a methionine surrogate, activating methionine tRNA synthetase and replacing methionine in proteins that are expressed in methionine-depleted media[58]. Consequently, methionine auxotrophs supplemented with AHA can be used to introduce azides at specific desired sites in proteins. Since methionine is the second rarest amino acid, there are few native sites to content with. To eliminate the initiator AHA, an alanine residue can be introduced at position 2, which results in its complete cleavage[59]. Once introduced into the protein, the azide can be conjugated to an alkyne through copper-catalyzed “click” chemistry or, with a strained alkyne, though copper-free cycloaddition[60]. Because strained-cyclooctyne fluorophores are commercially available and react without copper or ligand, we use this chemistry to attach the dyes and are free to reserve the cysteine residues for DNA handle attachment[26].

Labeling and functionalization is a multi-step process (Fig. 8, see Methods for further detail). For labeling to be specific, the protein under study must contain no accessible methionine or cysteine residues besides the labeling sites. Proteins are expressed in M15MA, a methionine auxotroph strain of *E. coli*[61], in M9AA media supplemented with $MgSO_4$, glucose, $CaCl_2$, thiamine, and the antibiotics ampicillin and kanamycin. The resulting azide-containing proteins can be purified using standard chromatographic procedures. For our samples, we include a His_6 tag, which allows purification using a Ni column. Purified protein is labeled with a four-fold excess of Alexa-555 DIBO and Alexa-647 DIBO dyes, then reduced with dithiothreitol (DTT), and then activated with dithiodipyridine (DTDP). DTDP activation promotes the subsequent conjugation to a thiol-modified oligonucleotide[26], generating a protein-ssDNA chimera. Two different oligonucleotides, each complementary to the thiol oligonucleotide but one with a biotin moiety and the other with a 4-bp phosphorylated overhang, are annealed to the chimera. This chimera is purified away from unreacted oligonucleotides by a second Ni purification. The resulting product is ligated to half-lambda phage DNA incorporating digoxigenin at one end and a complementary overhang at the other. The result is a mixture of species. With two protein azides and two different dyes, four different species are possible. Similarly, with two protein cysteines and two different DNA handles, four different chimeras are produced.

The use of two dual-labeling chemistries exploits some useful symmetry but also produces some undesirable species. For example, a protein labeled with a donor fluorophore at its first AHA position and an acceptor fluorophore at its second AHA position is assumed to behave the same as a protein labeled with a donor at its second position and an acceptor at its first, as the FRET is only a function of their distance. Similarly, a protein attached to a short DNA handle at its first cysteine position and a long handle at its second cysteine position is assumed to behave the same as a protein labeled with a short handle at its second position and a long handle at its first position, because the axis of force application remains the same. Proteins that conjugate to two short handles or two long handles will be unable to form tethers between a bead and the coverslip surface. They will be screened out during data collection. Similarly, proteins conjugated to two donor fluorophores or two acceptor fluorophores will not exhibit FRET; they must be screened out as well.

Chapter 4 – Instrument calibration

The hybrid instrument, like any other tool of force spectroscopy, measures molecular changes resulting from the application of force. It is crucial then that the magnitude of the applied force be accurately and precisely known in order to draw valid conclusions about its effect on a molecule. Unfortunately, the force applied by a magnetic tweezers depends on many factors that are variable and difficult to precisely predict *a priori*, such as magnetic field geometry, bead size and magnetic content, and microfluidic chamber dimensions; the predominant factor, the height of the magnet above the bead, follows no simple formula[62]. Because of this, the applied force is not calculated *a priori* but is instead determined by analyzing the motions of tethered beads that are subject to the applied force. This chapter will discuss how to calculate the applied force and construct a calibration curve using this method. The robustness of this calibration is subsequently evaluated by three independent methods.

A tethered magnetic bead within the magnetic field gradient of an external magnet exhibits lateral fluctuations whose variance scales inversely with the magnitude of the applied force and is proportional to the tether length and absolute temperature. This result from equipartition, $F=kbTl/<dx2>$, motivates a practical method for the calibration of a magnetic tweezers[54]. With the magnet at constant height and thus applying a constant force, observation of the constrained Brownian motions of a bead will yield the magnitude of the applied force. By repeating this process over a range of magnet heights, a calibration curve can be constructed. Any arbitrary force can then be applied by lowering the magnet to the appropriate height.

Unfortunately, the real process is not so straightforward, and a number of complications arise. First, an exact measure of the variance due to Brownian motion is only possible with an experimental detector possessing infinite bandwidth and an optical setup free of drift[63]. Bandwidth limitations and drift both have significant effects on the measured variance. Second, the effective length of a tether is never precisely known. Even though a DNA tether may have a well-defined contour length, its effective length will vary depending on where it attaches to a bead relative to the bead's preferred magnetic moment. The effective length also depends upon which lateral direction is considered. In the direction perpendicular to the magnetic field, the effective length includes the radius of the bead, which itself is subject to variation. Third, due to this variation in bead size, two beads on the same experimental setup will yield calibration curves that differ by a force-scaling constant, which has been found to vary as much as 20%. As a consequence, only a nominal force may be applied using a calibration curve. A precise force determination requires analysis of every individual bead. Each of these problems is considered in turn.

In order to determine the exact positional variance of a tethered bead, one would need to sample the position of the bead for an infinite time at an infinite rate. Anything less would miss some bead positions, resulting in an underestimate of the variance and an overestimate of the applied force. The most obvious manifestation of this finite exposure effect is camera blur. A frame acquired by a camera is not an instantaneous snapshot of the position of the bead but rather an average of positions over the exposure time. Consequently, rare, extreme positions are averaged with more common, central positions, artificially lowering the variance. Fortunately, beyond sufficiently fast sampling rates, most populated positions are sampled and subsequent samples of position become so strongly correlated that faster acquisition does not significantly change the variance. The same is true after a sufficiently long acquisition time; most positions have been sampled, so longer sampling has little effect on the measured variance. Thus, for practical purposes, determining the variance of a tethered bead is a matter of sampling fast enough, long enough.

How fast is fast enough and how long is long enough? These questions can be answered by analyzing the power spectrum of an acquisition. Brownian motion subject to a harmonic potential exhibits a characteristic power spectrum called a Lorentzian, the integral of which equals the variance. At low frequencies the power remains constant, but at high frequencies it decays to nothing. Two parameters, one that describes the initial power and one that describes the decay corner frequency, are sufficient to describe this power spectrum. Thus, the variance underestimate due to finite acquisition time can be calculated by integrating the constant initial power over all frequencies up to the inverse of the acquisition time. Similarly, the underestimate due to finite acquisition rate can be calculated by integrating the decaying power over all frequencies above the acquisition rate. An acquisition is fast enough and long enough if these underestimates are negligible. A general rule of thumb is that the acquisition rate must be at least four times the corner frequency. Error in the variance resulting from finite acquisition time should decrease according to $1/\sqrt{n}$, where n is the number of unique samples, which are spaced $1/(2\pi * f_0)$ apart. At 10 pN, the corner frequency, f_0, of a tether of half-lambda with a 2.8 μm bead is roughly 10 Hz. Consequently, for the work in this thesis a 100 Hz acquisition is taken for 2 min., resulting in 753,982 independent samples and 0.1% relative error.

While these guidelines minimize the error due to finite acquisition, there is an additional source of error that they do not correct for. Drift in the bead's position, which may result from thermal expansion, changes in air pressure, ground vibrations, etc., has the opposite effect of finite exposure, increasing the variance and resulting in an underestimation of the applied force. However, because this drift is only significant at low frequencies, below 0.05 Hz, it too may be identified through analysis of the power spectrum, manifesting as a departure from the constant initial power exhibiting by beads unaffected by drift. Fortunately, there is a sufficient sampling of frequencies unaffected by drift for the initial power to be fit, allowing the true variance to be extracted even from acquisitions of beads exhibiting drift.

An effective solution to calculate the variance free of the problems posed by finite acquisition and drift, and the one used in this research, is to fit the experimental power spectrum with a Lorentzian. Fitting in the frequency domain presents two fundamental advantages over direct calculation of the variance that ignores time. First, fitting allows the entire frequency domain, including that outside the observed range, to be considered for the calculation of the variance. While appropriate sampling can only minimize the variance missed due to finite sampling, fitting can effectively eliminate it. Second, by fitting only over the range of frequencies greater than 0.05 Hz, contributions to the variance arising from low-frequency drift can be excluded.

With the variance determined, the other variable that must be known to calculate the force is the length of the tether. Naively, the length of the tether should only depend on the length of the molecule tethering the bead. While the molecule length will depend on the applied force, DNA is known to follow the worm-like chain model, so the length and force could in principle be simultaneously determined through a bootstrapping procedure. Unfortunately, a larger factor affecting tether length is that tethered beads rotate into the applied magnet field in a way that brings them closer to the surface. This phenomenon occurs because the paramagnetic beads are not truly isotropic; they consist of ferrite or magnetite nanoparticles randomly dispersed in a polystyrene medium[64]. This random dispersion produces anisotropy that causes beads to have a preferred magnetic moment. Beads will rotate freely around this axis, but they will turn to align the moment with the applied field. A tether may attach to any point of the surface of the bead, but when a magnetic field is applied and the bead is pulled upward with the gradient, the attachment point will not necessarily re-orient to the point closest to the surface. Instead, the attachment point will be displaced some distance in the direction of the applied field, resulting in an effective tether that is shorter by as much as the radius of the bead. Since our beads have a radius of 1.4 μm and our half-lambda tethers are around 7.4 μm in length under force, this effect is significant.

The solution is to measure the height of a tethered bead directly. Most magnetic tweezers, which are predicated upon measuring changes is height, do this anyway. The procedure is detailed in the second chapter, and is accomplished by interpolating the diffraction pattern from the image of a defocused bead, creating a lookup table of images of a stationary bead taken at known defocused positions. A correction must also be made to account for the objective, as raising it a certain interval does not raise the focal height by the same interval. What is unique about the operation of the hybrid instrument is that the lookup table is constructed relative to a focal position where surface-bound fluorophores appear in focus. For a measurement of the length to be valid, it must be made with the focus on the surface as well. However, because the depth-of-field is not a single plane, the fluorophores will appear in focus over a narrow range of foci, and this contributes a small amount of error to a measured length. In practice, the same focus can be found within 30 nm, likely because there is a narrower range of foci that allows both red and green fluorophores to appear in focus. This 30 nm is small compared to the roughly 7.6 μm lengths typically measured and is thus considered negligible.

Another effect that must be accounted for is that the effective tether length is longer in the direction perpendicular to the applied field because it includes the radius of the bead. The uncertainty in the radius of the bead is relative small given the manufacturer coefficient of variation of 2-3%, so it may be safely assumed to be negligible, on the order of the error in length contributed by deviations in the focus. Thus, force is independently calculated for the directions parallel and perpendicular to the magnet field. A corrected length is used for the perpendicular direction, and the average of the two force calculations is used.

Constructing a calibration curve requires measuring the applied force across a range of high and low forces. As the applied force increases, so too does the corner

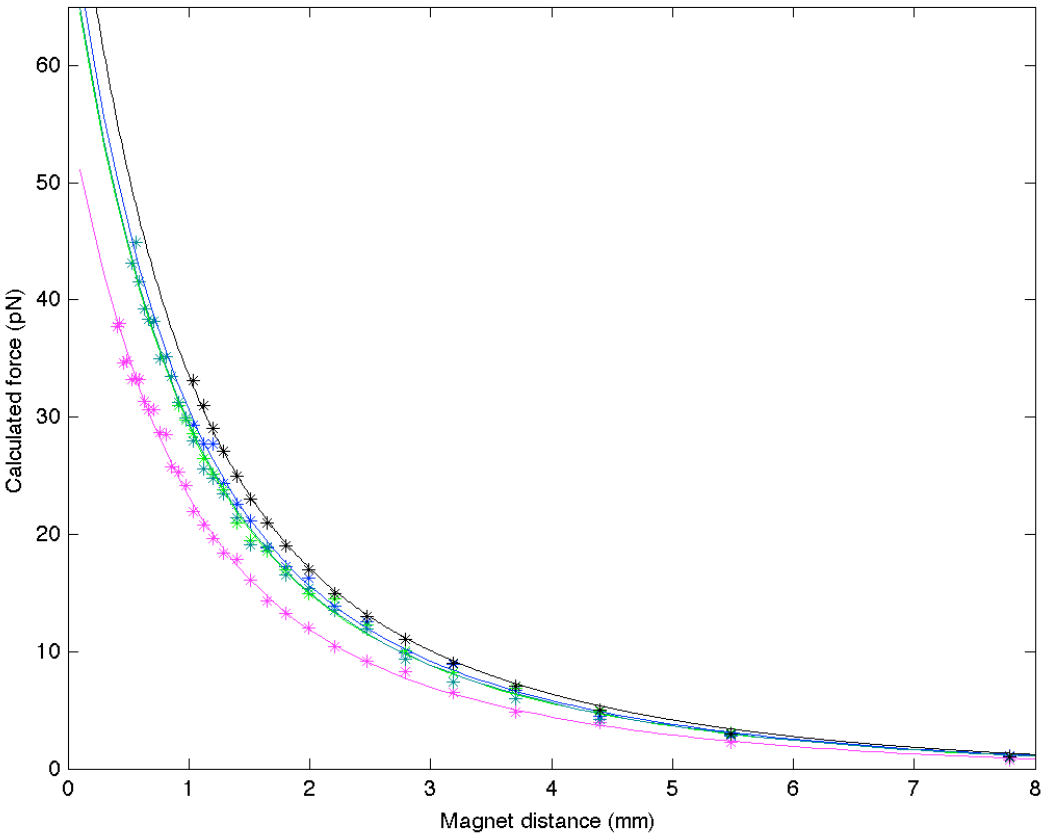

Figure 9. The magnet force-distance calibration curve. Five different tethered beads, each a different color, exhibit the same shape but differ by a scaling constant. Fit is $F=F_0*(a*\exp(-b*x)+c*\exp(-d*x))$, where a=48.54, b=1.376, c=30.13, and d=0.4054.

frequency of the bead, which increases the number of independent measurements made in a fixed acquisition time but also necessities higher sampling frequencies to minimize camera blur. Higher forces also diminish the magnitude of the variance, making precise determination more difficult. Fortunately, because the hybrid instrument possesses extremely high magnification in order to image single fluorophores, this last effect does not limit the range of forces that can be measured. It is necessary, though, to ensure that over the range of forces applied that the sampling frequency is still more than four times the corner frequency. For the system used in this research, consisting of half-lambda DNA and 2.8 μm diameter beads, the corner frequency reaches 25 Hz, a fourth of the 100 Hz sampling frequency, around 35 pN.

The shape of the calibration curve has been theoretically modeled and verified only for simple magnet geometries and not for the magnet used in the hybrid instrument. For two cubic neodymium magnets separated by a known gap distance, for example, the applied force decays exponentially. However, other researchers have reported needing a sum of two exponentials to model their magnetic tweezers. This deviation from single exponential behavior cannot be attributed to errors in force calibration arising at higher forces. The is true of the magnet used in the hybrid instrument as well, which may be due to its hybrid construction of six antiparallel NdFeB magnets with soft steel tips (Fig. 9).

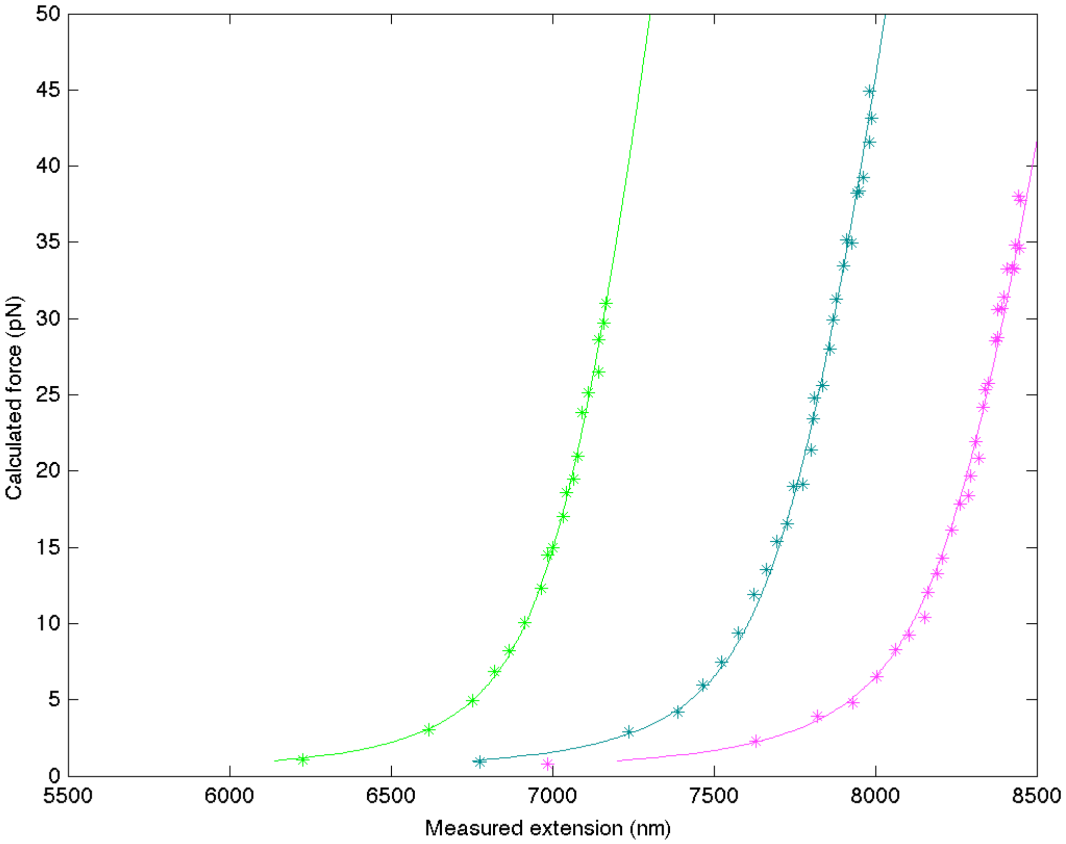

Figure 10. Worm-like chain force-extension behavior of three different tethered beads. Due to random off-center attachment of tethers to beads, the contour length of each tether will vary. However, each should exhibit the same persistence length of 50 nm.

While the calibration curve of magnet height is sufficient to capture the decay of the magnetic field gradient, it does not take into account the variation in bead size that makes a meaningful contribution to the force. We use Dynabeads M-280 magnetic beads (Thermo Fisher Sci.), which have a coefficient of variation of less than 3%. Although the diameter of the bead may vary by only 3%, this corresponds to a 27% variation in bead volume, the factor that is proportional to force. Consequently, the calibration curves from different beads on the same experimental setup will differ by a scaling factor of the same magnitude that accounts for this variation. In this research, a normalized calibration curve was constructed using a two-step process. First, the entire range of forces was measured for five different beads. These curves were fit globally with each allowed a floating scaling factor. In the second step, ten more tethered beads were measured at a single force. The distribution in scaling factors for all fifteen of these beads recapitulated that in the literature and displayed a coefficient of variation in line with the 3% reported by the manufacturer. This fifteen-bead sampling allows a better estimate of the average bead size than a random selection of five beads would, allowing the calibration curve to be normalized.

Because the exact force applied to a tethered bead will differ from the nominal force determined by the calibration curve, it is necessary to take a single force measurement of each bead from which data is collected. It is not known whether a tethered bead will yield useful fluorescence information until this data is collected, so

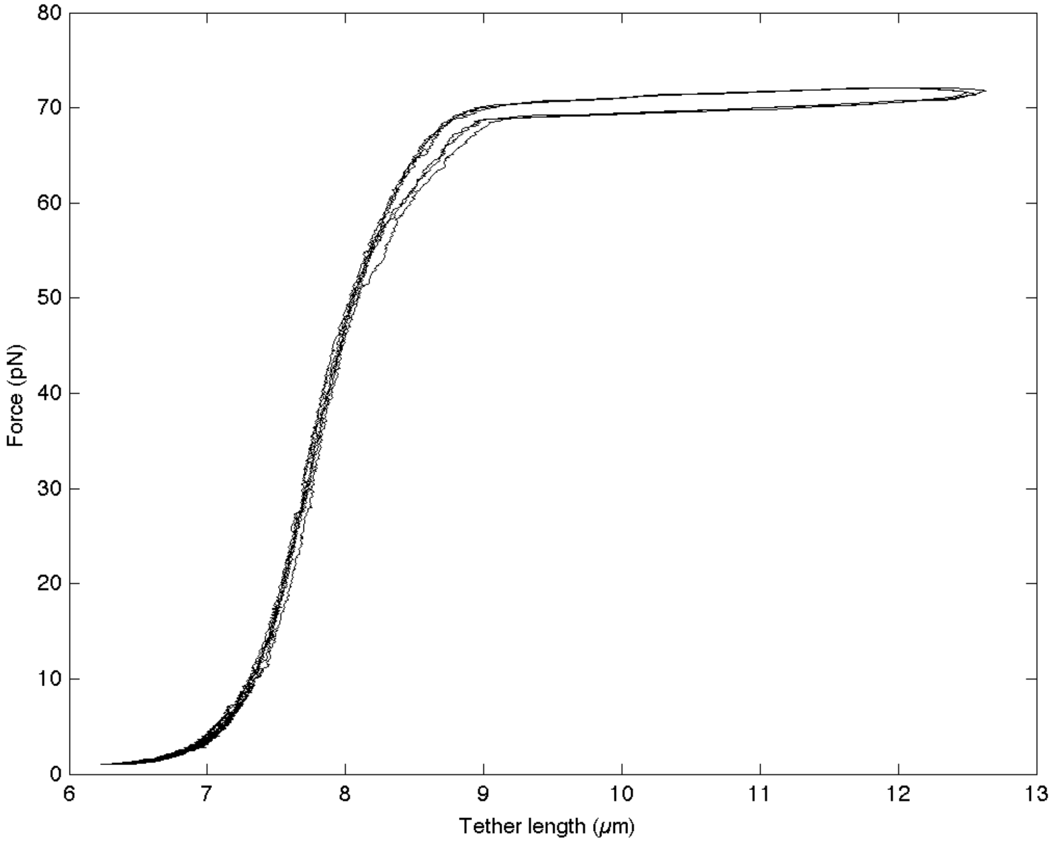

Figure 11. Overstretching of double-stranded DNA. At roughly 65 pN of applied force, a DNA tether exhibits a dramatic and reversible change in length.

this force measurement is made afterwards. Thus, molecules are subjected to nominal forces agnostic of the necessary force scaling, and this correction is only made during analysis. This highlights the importance of normalizing the calibration curve. The better the normalization, the closer on average the nominal applied force to the true applied force.

In order to verify that the force calibration has been properly carried out, it is important to test it against molecular systems with known force responses. Three different phenomena are measured here: the extension of double-stranded DNA, the overstretching of double-stranded DNA, and the hopping of DNA hairpins. It is well known that double-stranded DNA stretches under applied force according to a worm-like chain model with a persistence length of 50 nm. By measuring the length of a DNA tether over a range of applied forces, this property can be used to verify the proper calibration of both length and force measurement in the hybrid instrument. Conveniently, this is the same procedure that must carried out to construct the magnet height, so the same data from the five tethers may be used. While they exhibit a range of contour lengths, due to the shortening of tethers caused by the preferred magnetic moment of the beads discussed above, each tether exhibits a persistence length of 50 nm (Fig. 10).

A second force-dependent phenomenon that is useful for force calibration is the overstretching of DNA observed at 65 pN. This force is beyond the range of the

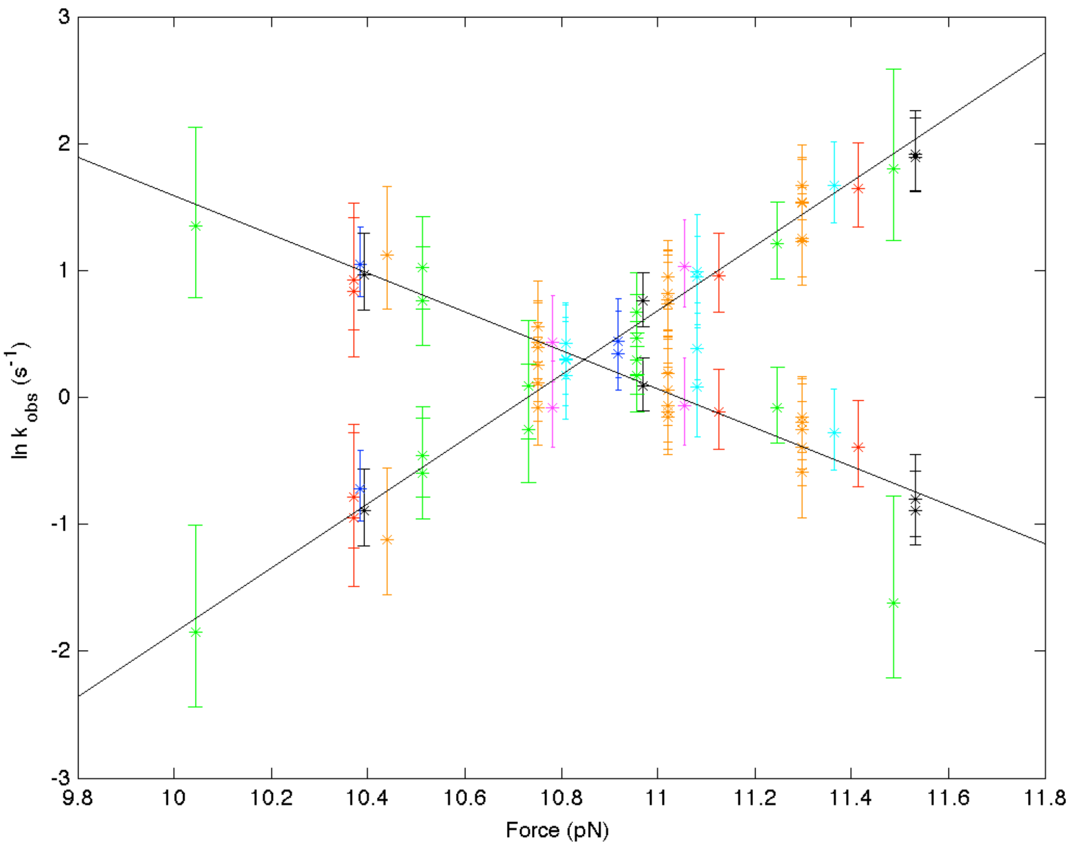

Figure 12. Kinetics of DNA hairpin opening and closing under force. Over a narrow range of force, the hairpin hops between open and closed states, allowing calculation of the kinetics of both opening and closing.

calibration curve, both because force measurements are subject to greater error at these corresponding high corner frequencies but also because the probability of tether breakage becomes significant over the acquisition times necessary to measure the force. Thus, 65 pN is extrapolated from the calibration curve, and is approached at a loading rate of 10 pN/s to minimize the chance of breakage. This extrapolation turns out to be sufficient, and a dramatic increase in length is observed at 65 pN (Fig. 11). This shows that the force calibration is reliable beyond the range directly measured and that the sum of exponentials is valid.

Our third independent calibration relies not only on the magnetic tweezers components but incorporates the fluorescence detection as well. A DNA hairpin, 15R60/T8, whose hopping kinetics were previously characterized using an optical tweezers[57], was functionalized with fluorophores according to the procedure detailed in chapter three. Rather than measuring the opening and closing of the hairpin from movements of the bead, the hopping between high and low FRET states was measured directly from the molecule itself (Fig. 12). The force at which open and closed states are equally populated, $F_{1/2}$, was found to be 10.8 pN, comparing well with the value of 10.3±0.5 pN observed in the optical tweezers study[57].

Chapter 5 – The effect of force on the alpha helix

Numerous proteins must exert, withstand, and yield to mechanical forces to carry out their functions. Because mechanical stability cannot generally be inferred from structural information and correlates poorly with thermodynamic stability, the mechanical properties of proteins must be studied using a force-spectroscopic technique like optical tweezers or atomic force microscopy[65]. Surprisingly, the unfolding/refolding transition of the alpha helix, the predominant element of protein structure, has heretofore evaded detection in these experiments, despite its ubiquity and direct implication in crucial force-dependent biological processes. Here, using a hybrid TIRF smFRET-magnetic tweezers instrument to probe fluorophore-labeled molecules, we establish both the force-induced unfolding/refolding signature of an isolated alpha helix and, for comparison, the force-extension behavior of an unstructured polypeptide. The helix-coil transition is rapid, allowing equilibrium measurements. It unfolds in a cooperative, continuous manner at 14 pN, while the unstructured polypeptide exhibits a steady, non-cooperative FRET decrease across the range of applied force, 1-30 pN. The former behavior explains the failure of force spectroscopic methods alone to detect the helix-coil transition and suggests that hybrid methods combining single-molecule optical or magnetic tweezers with simultaneous FRET detection may provide access to previously undetected features of the unfolding/refolding of globular proteins. Our results suggest that isolated alpha helices can be mechanically robust, unfolding in the same force range as many thermodynamically stable proteins.

Many biological processes are mechanical. Forces often develop in the course of biochemical reactions and the resulting protein stresses are important for signal transduction and communication in the cell[7,66]. An important participant in many of these processes is the alpha helix, an element of secondary structure with hydrogen bond interactions between the carbonyl group of residue *i* and the amide hydrogen of residue *i*+4, which constitutes nearly 30% of globular protein structure[1]. For example, the folding and assembly of alpha helices into coiled-coils provide the driving force for membrane fusion[9]. In general, the stability of an alpha helix depends on tertiary interactions; however, they have also been found in isolation, acting as linkers or rigid spacers between globular domains or, in the case of myosin VI, as force transducers[8]. Despite their importance, we know little about the mechanical properties of these canonical secondary-structural elements. What is their mechanical stability? That is, how much force can they withstand before undergoing denaturation? How cooperative is the force-induced helix-coil transition?

In the last two decades, single molecule force spectroscopy has become a powerful approach to study protein folding and to investigate the mechanical response of proteins[10,11,22]. Experiments using optical tweezers indicate that under mechanical tension, small, single-domain globular proteins usually unfold in a single transition between ~5-50 pN, depending on pulling geometry, topology, and sequence[13,21]. This single unfolding transition suggests that secondary and tertiary structures are simultaneously disrupted, as no separate signature for helix unfolding is observed and the transition accounts for the total expected contour length of the molecule. Thus, helical segments of the typical length found in proteins are not expected to resist forces much greater than 5 pN. Recent work from Rief and coworkers, however, suggests that a 25-residue helix of myomesin remains folded up to 30 pN[47]. Thus, the force at which an alpha helix unfolds might vary substantially depending on length and sequence. Is the unfolding of globular domains so cooperative and the stability of alpha helices so dependent on tertiary structure that no residual secondary-structure elements remain after the force-induced disruption of globular structure? Equivalently, in terms of folding, can certain secondary-structural elements form before hydrophobic collapse?

Even if present, several technical reasons may prevent the observation of a recognizable helix-coil transition during the mechanically induced unfolding/refolding of a protein. First, the helix-coil transition is rapid and not necessarily two-state– any measurement is likely to represent an equilibrium average of helical content that decreases continuously as the force is increased. This continuous behavior may be difficult to deconvolute from the force-extension associated with the unfolded polypeptide or from the DNA handles often used in optical tweezers experiments. Second, the expected extension change for helix unfolding is small, especially if it occurs at low forces. Assuming the unfolded state obeys an inextensible worm-like chain with a persistence length of 6.5 Å[25,67], the expected extension change per residue would be only 1.5 Å at 50 pN and vanishingly small at 4.9 pN. Given that the average helical segment in globular proteins is ~12 amino acids[50,51], unfolding would produce an extension on the order of 1 nm. Detecting this extension at an unknown force against the background of a continuously extending random coil would be a challenge for even the highest spatial-resolution methods of force spectroscopy. As a result, it would not have been possible to characterize the force-induced helix-coil transition of isolated alpha helices or to observe the piece-wise unfolding of a globular protein even if these secondary structures were present.

In order to circumvent these difficulties, we have developed a hybrid magnetic-tweezers-single molecule FRET assay using TIRF excitation geometry and a novel labeling methodology (Fig. 13a). We apply force across a hundred-residue alanine-based peptide that forms a stable helix in the absence of force. We selectively label two residues separated by 24 amino acids with donor and acceptor dyes and monitor the conformational change of the molecule via changes in the FRET signal. This provides subnanometer resolution of the peptide's extension, independent of the DNA handles and beads, and allows detection of a helix-coil transition. These results are compared to the force-extension characteristics of a molecule in which sixteen residues have been replaced by glycine to prevent formation of an alpha helix in order to evaluate the unfolded state under the same conditions.

The model helix studied here is based on canonical isolated alpha helices, alanine-based peptides interspersed with lysine and glutamic acid to provide charge-balanced solubility[3,4,68,69]. While peptides as short as 14 residues exhibit some helicity, we use 90 residues to minimize fraying at the termini and maximize helicity (Extended Data Fig. 1). Force is applied through DNA handles that are attached to two cysteine residues near the ends of the helical sequence. Purification tags are outside these cysteine residues. The fluorescent dyes are incorporated using the unnatural amino acid azidohomoalananine (see Methods). The resulting construct was demonstrated to be

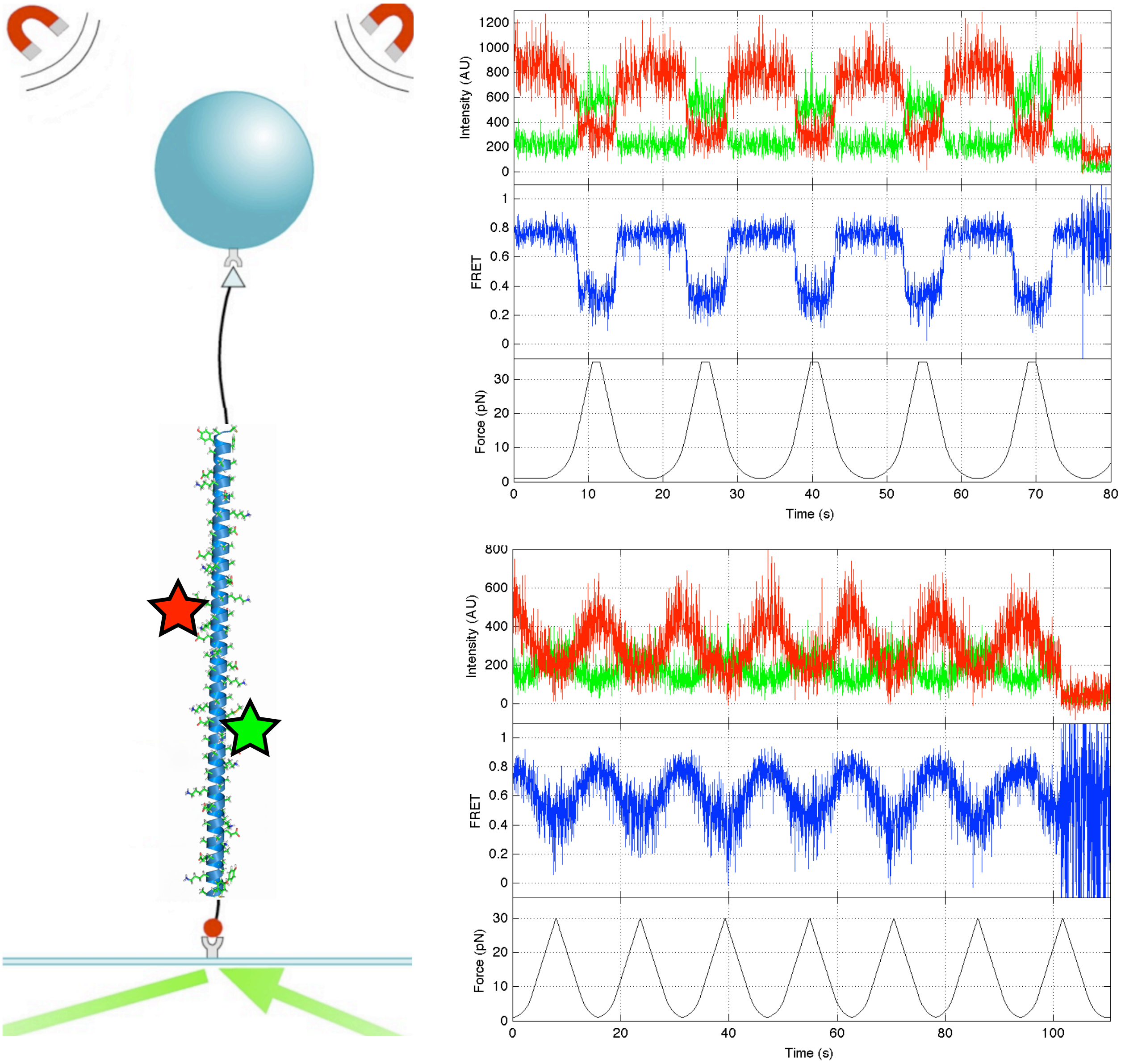

Figure 13. Experimental setup and single trajectories. Left: A single isolated alpha helix is conjugated to two FRET-paired small molecule fluorophores and to two DNA handles, one short (20 bp) and one long (24 kbp), that tether it between a passivated coverslip and a paramagnetic bead inside a microfluidic chamber. Force is applied by modulating the height an external permanent magnet, resulting in conformational changes that can be detected in an objective-TIRF configured fluorescence microscope. Right, top: Example trajectory of an alpha helix tether. Right, bottom: Example trajectory of an unstructured polypeptide.

helical by circular dichroism, as predicted by the AGADIR algorithm (Extended Data Figs. 2-4)[6,70-73].

Twelve individual molecules were evaluated using multiple pulling cycles on the magnetic tweezers-fluorescence instrument for a total of 124 pulls. Each tether showed similar behavior (Fig. 13b). At low force, all tethers showed a constant FRET value of ~0.8. At ~10 pN to ~18 pN, the FRET signal decreased rapidly to a value of ~0.4. Above this, as the force was ramped to 30 pN, the FRET signal decreased only slightly. This sigmoidal FRET change was reversible and repeatable, with subsequent pulling/relaxation cycles yielding the same FRET values at any given force. These

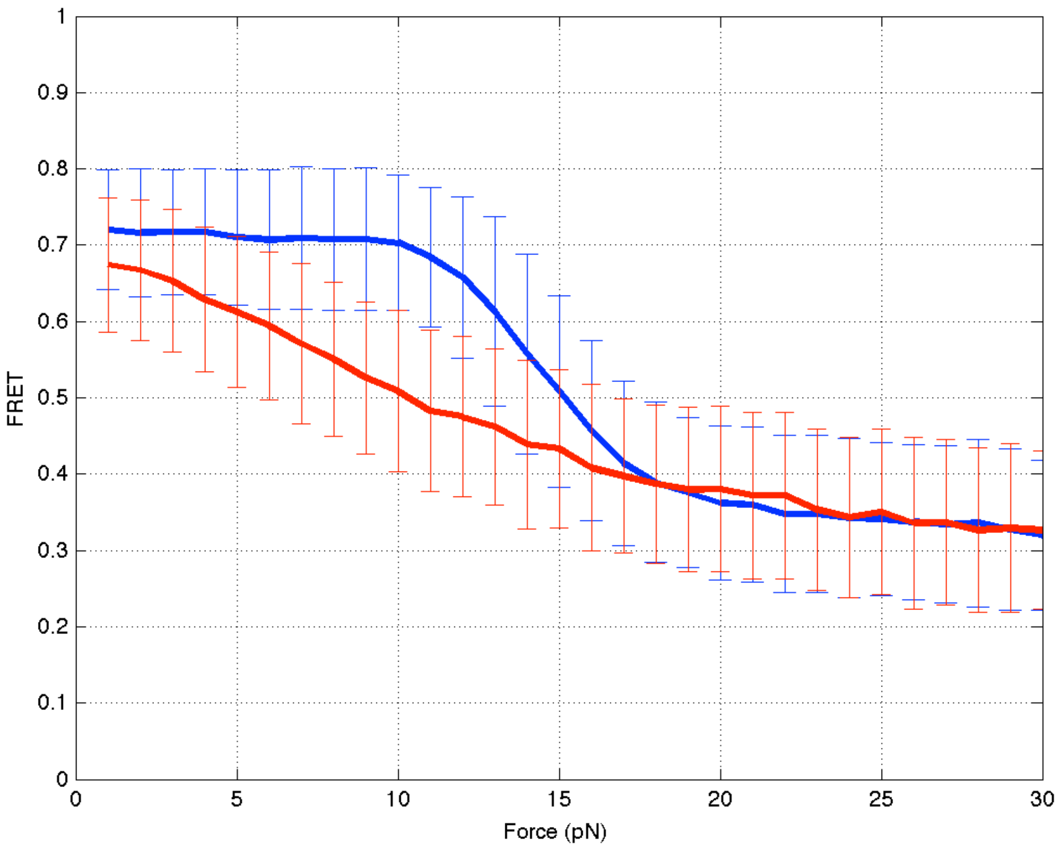

Figure 14. Comparison of average alpha helix and unstructured polypeptide force-FRET behaviors. The alpha helix (blue) exhibits a sharp, reversible decrease in FRET with a midpoint at 14 pN. The polypeptide (red) exhibits monotonically decreasing FRET as force is applied that overlaps with that of the alpha helix at forces above 17 pN.

FRET signals were independent of the loading rate, with cycles at 5 pN/s and 10 pN/s superimposing (Fig. 14). The same behavior was seen in samples with and without the encoded purification tag.

In order to verify that the observed sigmoidal signal change reports on the helix-coil transition, a second construct was made to probe the behavior of unstructured polypeptide by replacing each lysine residue with glycine (Extended Data Fig. 1). The AGADIR algorithm predicts that these mutations will annihilate helical structure across the entire peptide (Extended Data Fig. 2); this was confirmed by circular dichroism (Extended Data Fig. 3). Qualitatively different force-induced FRET behavior was observed for this unfolded peptide (Fig. 13c). Application of force caused the FRET to decrease roughly linearly from 1 to 18 pN, beyond which there is a slight, monotonic decrease in signal. This change in FRET was also reversible and repeatable in subsequent pulling cycles and across 14 different tethers and 123 pulling cycles (Fig. 14). On occasion, these tethers exhibited pulling cycles where FRET remained constant at ~0.8 as increasing force was applied, followed by a discrete drop. The rest of the cycles showed the monotonically changing FRET typical of most of the unstructured polypeptide pulling cycles. The nature of this rare, but notable, anomalous behavior is not known, but is likely due to adsorption of the unfolded polypeptide chain on the

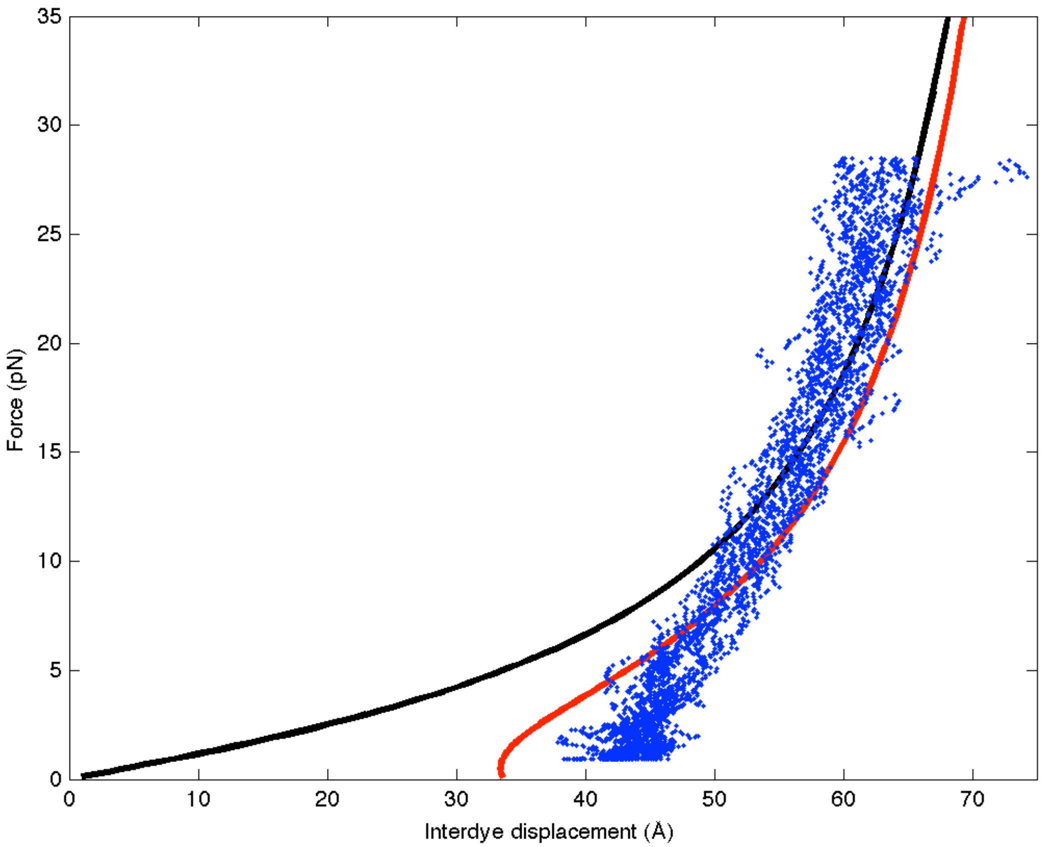

Figure 15 . FRET from a worm-like chain. The often-used expression for the worm-like chain (persistence length 6.5 Å, contour length 87.7 Å, black) gives the average extension along the axis of applied force, which is not what FRET reports. Our experimental FRET data of the unfolded peptide (blue) exhibit a signal related to the root mean square displacement (RMSD) between the dyes. The worm-like chain can be transformed, providing a relationship between force and this RMSD (red) that agrees with the experimental data: $\langle r^2 \rangle = z^2 + 2k_bTz/F + 2PL_0/(2+(1-z/L_0)^{-3})$, where $\langle r^2 \rangle$ is the mean square displacement, z is the average extension along the axis of applied force, F is the applied force, P is the persistence length, L_0 is the contour length, and k_bT is the thermal energy.

coverslip surface at low force. Consistent with this, we never observe this unusual behavior when we keep the force above 3 pN.

The steady, noncooperative decrease in FRET usually seen in the unstructured construct differs clearly and qualitatively from the cooperative decrease in the helical construct and can be modeled using a modified worm-like chain (WLC) analysis. Usually, the WLC model is expressed in terms of the average extension projected along the axis of applied force. For a direct comparison to FRET data, however, we have modified this to express the WLC in terms of the root mean square displacement (Fig. 15). Interestingly, while the model and experimental FRET agree very well at high forces, the experimental FRET indicates a more extended state at low force than the model predicts. While this discrepancy may be due to uncertainty and assumptions made in calculating FRET and absolute distance from fluorescence intensity (see Methods)[74,75], it may also arise from self-exclusion not considered in the model that reveals something about the nature of the unfolded state.

In sum, these data indicate that we have successfully developed a method that is sensitive enough to measure subnanometer conformational changes resulting from applied force. We have captured, for the first time, the reversible force-induced helix coil transition. To our knowledge, this is the first study to observe the force-induced conformational changes of any FRET-labeled polypeptide, and as such, offers unprecedented distance resolution of its low-force behavior.

The lack of hysteresis during the pulling cycles and their insensitivity to loading rate suggest that the helix is always at a force-dependent equilibrium and that the observed FRET is an average of those states populated at that equilibrium with an $F_{1/2}$ for the unfolding transition of ~14 pN. This unusual mechanical stability is initially surprising, since many proteins have been shown to unfold at forces lower than 14 pN. These protein unfolding transitions account for the entire expected contour length change, implying that the helical segments are unfolded. Apomyoglobin, for example, an entirely helical protein, unfolds reversibly at ~4.5 pN to its full contour length. This raises the question of whether the helical unfolding force observed here is high because its specific amino acid sequence and composition or because it is much longer than most protein-sized helices.

While the observed unfolding force (14 pN) is higher than expected based on protein studies, it is significantly lower than that suggested by recent computational studies using a modified AGADIR algorithm to incorporate the effect of force[76]. AGADIR is a helical prediction algorithm that augments a statistical mechanical treatment of a helix with empirical data. Torabi and Schatz modified this algorithm by incorporating force-extension terms. This modified algorithm predicts that our helical construct would unfold at 28 pN, even higher than what we observe. However, the model of the unfolded state they use is an inhomogeneous partially freely rotating chain that is less extended than the more commonly used worm-like chain. This results in an underestimation of the effect of force. When we adapt their algorithm to incorporate a worm-like chain with a persistence length of 6.5 Å, the unfolding force drops to 17 pN (Fig. 16). The small remaining discrepancy has two possible explanations: (1) AGADIR predicts a high zero-force helicity than experimentally observed (Extended Data Fig. 4) or (2) the true persistence length is slightly larger than 6.5 Å.

The hybrid smFRET-tweezers method we present here should enable the study of many protein systems not amenable to conventional force spectroscopy. We exploited the capability of FRET to probe subnanometer changes independent of the handles and beads, but more generally, this method allows dyes to be positioned independently of the pulling points, a crucial capability for investigating the allosteric nature of proteins.

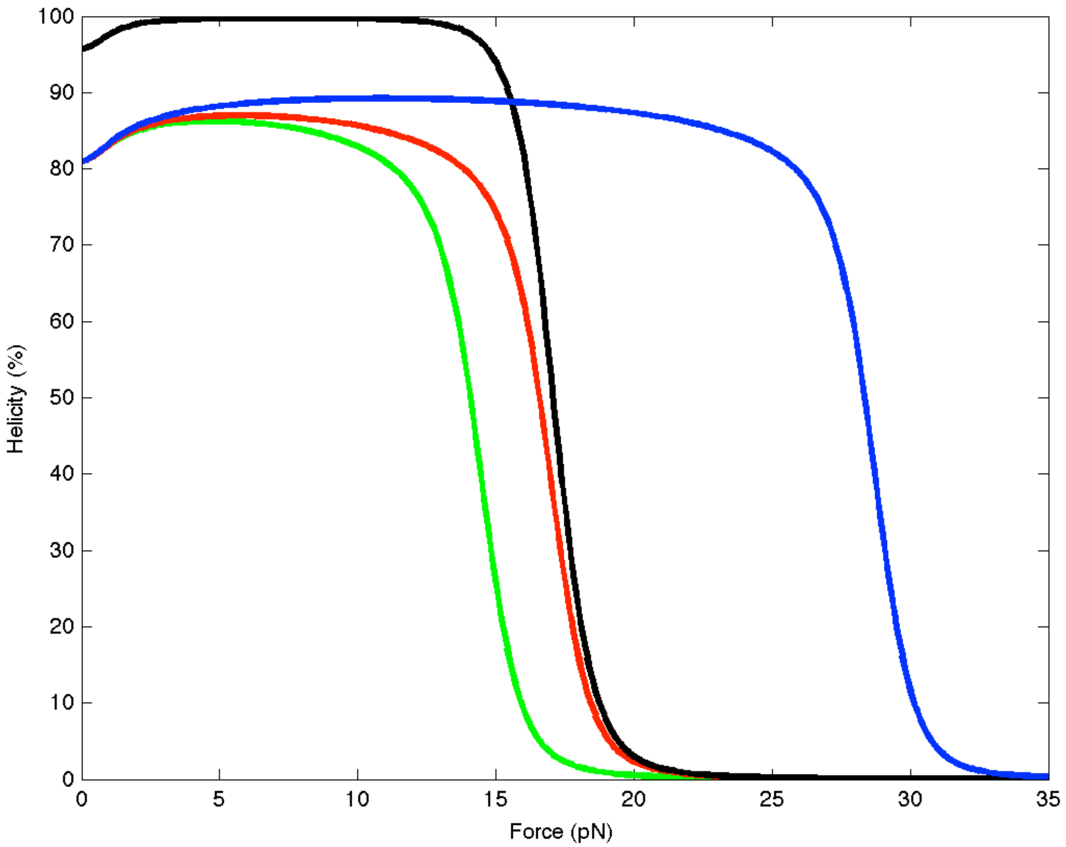

Figure 16. Helicity predicted by AGADIR incorporating force. When the inhomogenous partially freely rotating chain is used as the model of the unfolded state, AGADIR predicts the helical construct will unfold at 28 pN (blue). In contrast, using the worm-like chain with a persistence length of 6.5 Å (red) predicts a midpoint force of 18 pN. Increasing the persistence length to 8.0 Å (green) decreases this force further to 14 pN. Considering the helicity only of residues between dye attachment points for the WLC model (black) has a marginal effect on the predicted midpoint force.

Helix-MBP

GACAYYGAKAAEAAKAAEAAKAAEAAKAAEAAKAAEAAKAZEAAKAAEAAKAAEAAKAZEAAKAAEAAKAA
EAAKAAEAAKAAEAAKAAEAAKGYYACGSSHHHHHH

Helix+MBP

GSSHHHHHHGSSLKIEEGKLVIWINGDKGYNGLAEVGKKFEKDTGIKVTVEHPDKLEEKFPQVAATGDGPDIIFWAH
DRFGGYAQSGLLAEITPDKAFQDKLYPFTWDAVRYNGKLIAYPIAVEALSLIYNKDLLPNPPKTWEEIPALDKELKA
KGKSALLFNLQEPYFTWPLIAADGGYAFKYENGKYDIKDVGVDNAGAKAGLTFLVDLIKNKHLNADTDYSIAEAAFN
KGETALTINGPWAWSNIDTSKVNYGVTVLPTFKGQPSKPFVGVLSAGINAASPNKELAKEFLENYLLTDEGLEAVNK
DKPLGAVALKSYEEELAKDPRIAATLENAQKGEILPNIPQLSAFWYAVRTAVINAASGRQTVDEALKDAQTNSSSNN
NNNNNNNNLGIEENLYFQGACAYYGAKAAEAAKAAEAAKAAEAAKAAEAAKAAEAAKAZEAAKAAEAAKAAEAAKAA
EAAKAZEAAKAAEAAKAAEAAKAAEAAKAAEAAKAAEAAKGYYAC

Coil-MBP

GACAYYGAGAAEAAGAAEAAGAAEAAGAAEAAGAAEAAGAZEAAGAAEAAGAAEAAGAZEAAGAAEAAGAA
EAAGAAEAAGAAEAAGAAEAAGGYYACGSSHHHHHH

Coil+MBP

GSSHHHHHHGSSLKIEEGKLVIWINGDKGYNGLAEVGKKFEKDTGIKVTVEHPDKLEEKFPQVAATGDGPDIIFWAH
DRFGGYAQSGLLAEITPDKAFQDKLYPFTWDAVRYNGKLIAYPIAVEALSLIYNKDLLPNPPKTWEEIPALDKELKA
KGKSALLFNLQEPYFTWPLIAADGGYAFKYENGKYDIKDVGVDNAGAKAGLTFLVDLIKNKHLNADTDYSIAEAAFN
KGETALTINGPWAWSNIDTSKVNYGVTVLPTFKGQPSKPFVGVLSAGINAASPNKELAKEFLENYLLTDEGLEAVNK
DKPLGAVALKSYEEELAKDPRIAATLENAQKGEILPNIPQLSAFWYAVRTAVINAASGRQTVDEALKDAQTNSSSNN
NNNNNNNNLGIEENLYFQGACAYYGAGAAEAAGAAEAAGAAEAAGAAEAAGAAEAAGAZEAAGAAEAAGAAEAAGAA
EAAGAZEAAGAAEAAGAAEAAGAAEAAGAAEAAGAAEAAGGYYAC

Extended Data Figure 1. Amino acid sequences of the constructs studied in this research. DNA handles are attached to cysteine residues (cyan). Dyes are attached to azidohomoalanine residues incorporated in place of methionine residues (magenta). Initial methionine/azidohomoalanine residues are cleaved *in vivo*.

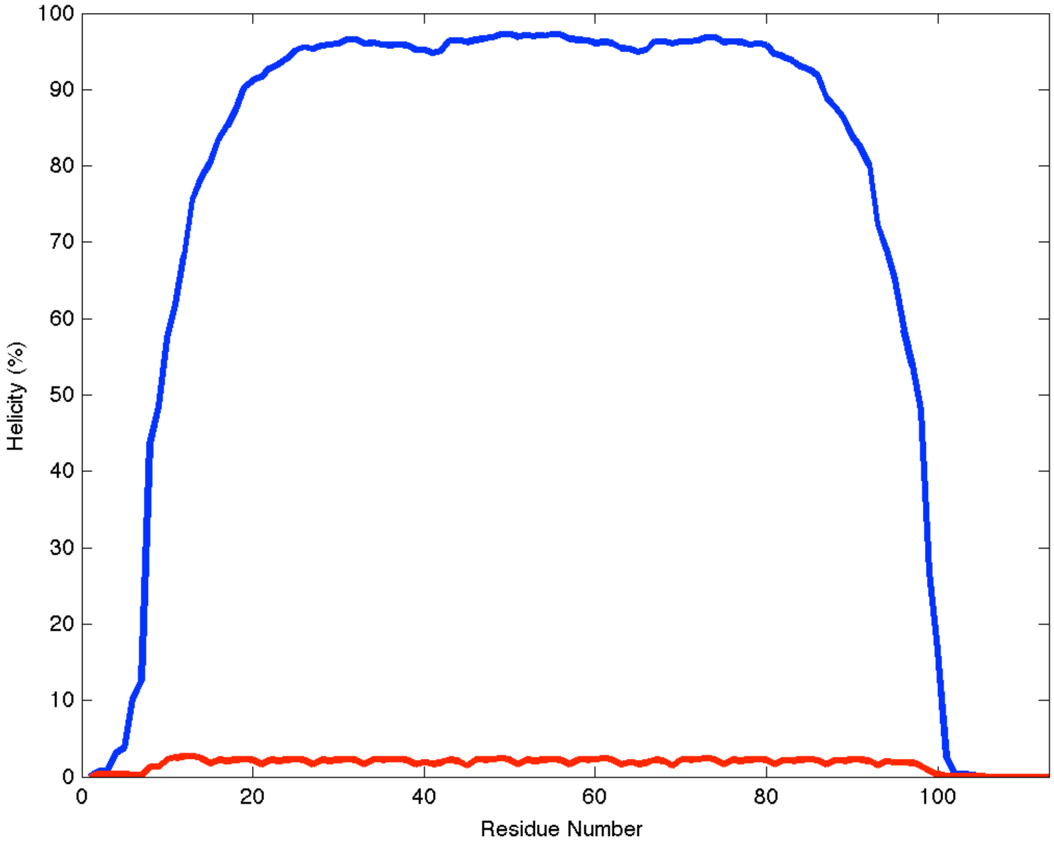

Extended Data Figure 2. AGADIR predicted helicity of helical (blue) and unstructured polypeptide (red) constructs.

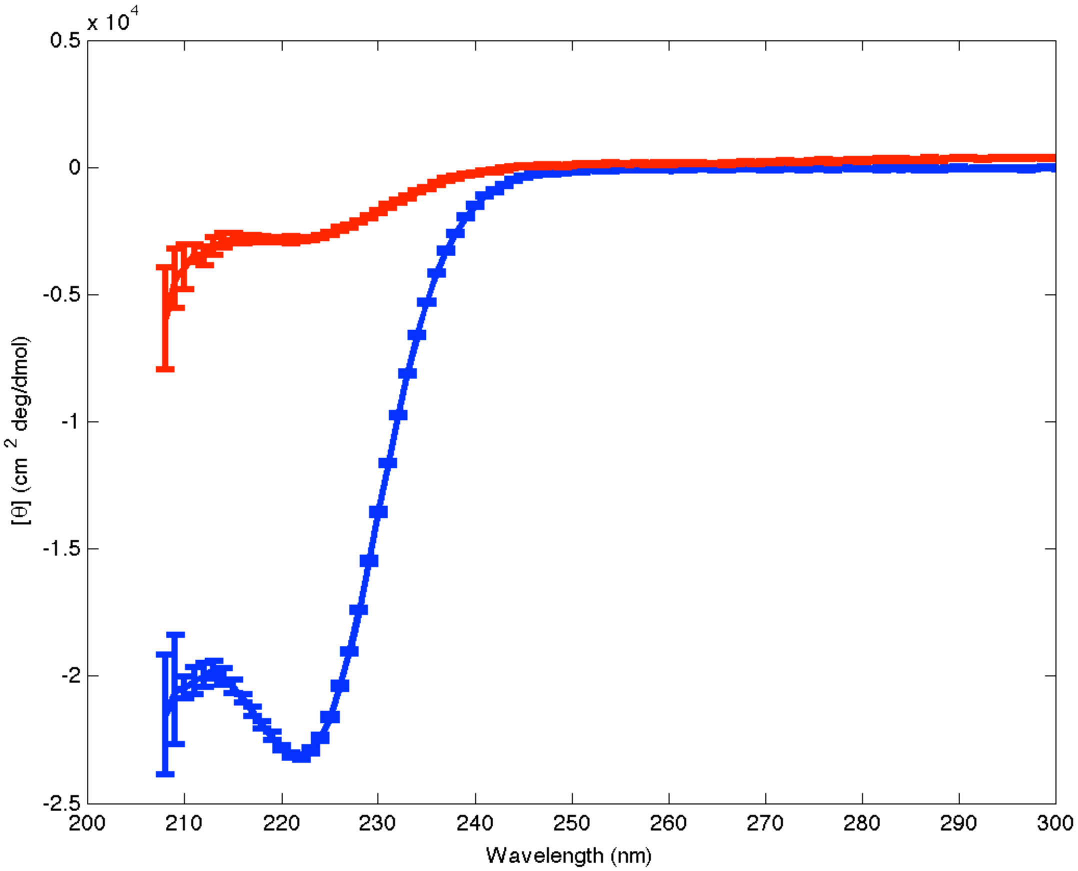

Extended Data Figure 3. Circular dichroism spectra of helical (blue) and unstructured polypeptide constructs (red).

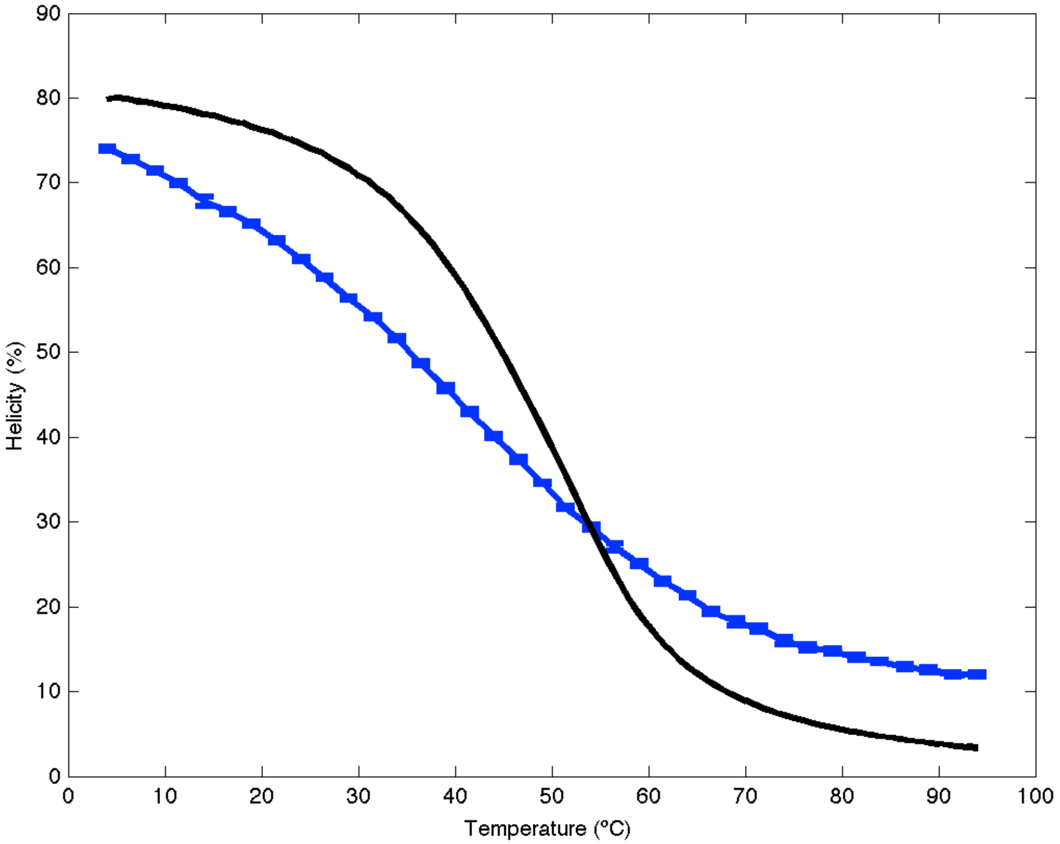

Extended Data Figure 4. Temperature melt of helical construct as determined by circular dichroism (blue) and AGADIR prediction (black). Helicity is calculated from [θ]*100/(-39500*(1-2.57/112)).

Methods

Cloning, protein expression, and purification

Plasmids encoding the protein constructs (Extended Data Fig. 1) were constructed with a pQE-60 background (Qiagen) using commercial oligonucleotide synthesis and standard molecular cloning techniques. For each of the helical and unstructured polypeptide designs, two versions were created, one with an N-terminal $(His)_6$-tag followed by maltose-binding protein (MBP) and a tobacco etch (TEV) protease cleavage site, and another with a C-terminal $(His)_6$-tag. All codons for methionine in the MBP sequence were mutated to leucine to prevent undesired azidohomoalanine and dye incorporation. Every construct incorporated a glycine residue in the second position to maximize cleavage of the initial methionine/azidohomoalanine during expression.

Constructs were transformed into and expressed in the methionine auxotroph M15MA strain of *E. coil*, a gift from the lab of C. Bertozzi, using a method adapted from Kiick et al[58]. Cultures were grown at 37 °C in 250 mL M9AA media supplemented with $MgSO_4$, glucose, $CaCl_2$, thiamine, and the antibiotics ampicillin and kanamycin. After reaching $OD_{600}=1$, cells were pelleted by centrifugation and washed at 4 °C with the same volume of 0.9% w/v NaCl twice. After a third sedimentation, cells were resuspended in an identical volume of M9AA media lacking methionine and permitted to grow for ten more minutes at 37 °C before addition of 50 mg azidohomoalanine. After ten more minutes, cells were induced with 1 mM isopropyl β-D-thiogalactopyranoside (IPTG) and harvested after 5 hours.

Cell pellets were resuspended in 50 mL 50 mM Tris, pH 7.6, 200 mM NaCl, 1 mM dithiothreitol (DTT), and 5 mM imidazole. Cells were lysed by sonication and pelleted, and the protein of interest was purified from the supernatant using Ni chromatography with a gradient of elution buffer containing 500 mM imidazole. Fractions containing the protein of interest were determined by SDS-PAGE, pooled, and concentrated to roughly 1 mg/mL using Amicon Ultra 4 mL 3kDa MWCO Centrifugal Filters (EMD Millipore). Protein concentrate not immediately labeled was diluted with 25% glycerol and stored at -20 °C.

Labeling and handle attachment

Alexa-555 DIBO and Alexa-647 Click-iT DIBO dyes (Life Tech.) were resuspended to 10 mM in DMSO and added to an aliquot of purified protein at a 4:1 molar excess of each dye for a final volume of 130 μL. After four hours at room temperature, 10 mM DTT was added. After two more hours, the labeling solution was exchanged into 50 mM Tris, pH 7.6, 200 mM NaCl using two successive Zeba 0.5 mL 7kDa MWCO Spin Desalting Columns (Thermo Sci.). Dye incorporation was measured using a NanoDrop spectrophometer (Thermo Sci.). Dithiodipyridine (Siga-Aldrich), prepared fresh as a 200 μM stock solution in acetonitrile, was then added in 50-fold molar excess and allowed to react overnight.

A commercially synthesized DNA oligonucleotide with the sequence GCTACCGTAATTGAGACCAC and a 5' thiol modification (Integrated DNA Tech.) was treated with a 100-fold excess of DTT and passed through two successive PD-10 columns (GE Healthcare Life Sci.) to remove the protecting group. An aliquot sufficient for a 6:1 molar excess of oligonucleotide to labeled protein was freshly reduced with 10 mM DTT for two hours and exchanged into 50 mM Tris, pH 7.6, 200 mM through two successive Zeba columns. The activated, labeled protein was exchanged out of excess DTDP and into identical buffer through two more successive Zeba columns, and the two were combined for four hours at room temperature. The extent of handle attachment was determined by gel shift of the fluorophore-labeled protein visualized on a Typhoon Trio fluorescence imager (Amersham Bio.). Two additional oligonucleotides, one with the sequence GTGGTCTCAATTACGGTAGC and a 5'-biotin moiety and another with the sequence CTAGGTGGTCTCAATTACGGTAGC and 5'-phosphorylation were each added in 2-fold molar excess to the thiol oligonucleotide and annealed to it by heating to 90 °C for three minutes and cooling slowly to room temperature. Functionalized proteins were purified from excess DNA oligonucleotides by Ni bead pulldown and elution in imidazole buffer.

Lambda phage DNA (New England Biolabs) was heated to melt *cos* sites and subsequently filled in with dATP, dCTP, dGTP, and digoxigenin-11-dUTP (Roche) using klenow fragment (NEB). It was then digested with XbaI (NEB) to create two roughly equal pieces. Excess nucleotides and enzymes were removed through purification on silica spin columns (Qiagen). This half-lambda fragment was ligated to the labeled, oligonucleotide-conjugated, Ni-purified proteins in DTT-free ligase buffer to create the functional construct. Treating MBP-fusion constructs with TEV protease at this point was not shown to change their force-FRET behavior.

Magnetic tweezers-TIRF smFRET spectroscopy

An IX71 inverted fluorescence microscope (Olympus) was fitted with a 100x 1.4NA UPlanSApo oil immersion objective (Olympus) and a motorized XY stage (Prior). A circularly polarized 532 nm solid-state laser (CrystaLaser) at 8.75 mW was aligned in an overfilling objective-TIRF configuration. A custom-built dual-view system separated donor and acceptor channels onto an EMCCD camera (Andor Tech.). A custom-built magnet was mounted on motorized translation and rotary stages (Physik Instrumente) above the sample. Magnetic beads were imaged using transillumination from an infrared LED (Roithner Lasertechnik GmbH) visible in the acceptor channel. Focal position was maintained using a CRISP Autofocus System (Applied Scientific Instrumentation) and an E-662 position servo-controller (Physik Instrumente). Components were controlled using custom LabVIEW software (National Instruments).

Microfluidic chambers were passivated and constructed using the method of Roy, *et al.*[52] Assembled chambers were injected with 40 mM Tris, pH 8.0, 250 mM NaCl, and 0.1% Tween-20, followed by 0.2 mg/mL streptavidin in the same buffer. After five minutes, unbound streptavidin was rinsed out with fluorescence buffer containing Tris, NaCl, and Tween-20; 4 mM Trolox, 2 mM 4-nitrobenzyl alcohol, and 2 mM cyclooctatetraene, as triplet-state quenchers; and 3 μg/mL glucose oxidase, 0.4 μg/mL catalase, and 0.8% glucose, as an oxygen scavenging system (all from Sigma-Aldrich). Functionalized molecule diluted to 50 pM in fluorescence buffer was then injected and rinsed out after five minutes. Finally, Dynabeads M-280 microspheres (Thermo Fisher Sci.) coated in anti-digoxigenin (Abcam) and diluted 1:100 in fluorescence buffer were injected. Inlets and outlets were sealed with epoxy for fifteen minutes before measurements were made.

Acquisitions followed a four-step procedure. First, with the magnet applying a nominal force of 1 pN, the surface of the coverslip was scanned under brightfield infrared transillumination to identify a defocused bead tethered by half-lambda DNA. Next, using TIRF, the apparent tether attachment point was checked for acceptor fluorescence, and therefore, proper labeling. A movie was then recorded while the force was ramped up and down and, if a change in FRET was observed, continued until the molecule photobleached. Finally, the Brownian motions of the bead were recorded under infrared transillumination at a nominal force of 10 pN for two minutes to correct for variation in bead size.

Analysis

TIRF movies were converted to trajectories of donor and acceptor fluorescence intensity using the smFRET analysis package published by the T. Ha lab[52] and *TwoTone*[77]. FRET efficiency was calculated using the equation $E_{\mathrm{FRET}}=(I_{\mathrm{A}}-\beta I_{\mathrm{D}})/(I_{\mathrm{A}}-\beta I_{\mathrm{D}}+\gamma I_{D})$, where I_{D} and I_{A} are acceptor and donor intensities, respectively, β is the leakage of donor fluorescence into the acceptor channel, and γ is the apparent ratio of dye quantum yield scaled by detection efficiency. Leakage was measured from untethered donor-only molecules as 0.14; this value was used for all tethered molecules. Gamma was measured from the relative acceptor/donor intensity change following acceptor photobleaching of untethered, dual-labeled molecules as 1.64 with a standard deviation of 0.60. Gamma values for tethered molecules of a given construct were subsequently fit to minimize square deviations in FRET, subject to an average of 1.64; the resulting distributions had standard deviations of 0.25 for the helical construct and 0.28 for the unstructured construct. No direct excitation of acceptor fluorophores was detected. Inter-dye distance was calculated from $R=(1/E_{FRET}-1)^{-6}*R_0$, where the Förster radius R_0 supplied by the manufacturer, 51 Å, was used.

XYZ positions of defocused beads were determined from movies using the quadrant-interpolation algorithm and a correction for the oil immersion objective[55]. Applied force was calculated by fitting a Lorentzian to the power spectrum to determine the corner frequency f_0 and initial power S_0 and using the relationship $F=2k_B Tl/(\pi S_0 f_0)$, where l is the measured tether length. Force scaling constants were determined for each bead to correct for variations in size and were multiplied by nominal forces from a magnet height-force calibration curve.

Circular dichroism spectroscopy

Measurements of circular dichroism were carried out on an Aviv 410 in a 1-cm pathlength curvette at protein concentrations of 50 μg/mL in 40 mM Tris, pH 8.0, 250 mM NaCl. No difference was observed when 0.8% glucose and 0.1% Tween-20 were added. No measurements could be made in the presence of the triple-state quenchers, due to their high UV absorbance.

References

1. Doig, A. J. Stability and design of alpha-helical peptides. *Prog Mol Biol Transl Sci* **83,** 1–52 (2008).
2. Bierzynski, A., Kim, P. S. & Baldwin, R. L. A salt bridge stabilizes the helix formed by isolated C-peptide of RNase A. *Proc Natl Acad Sci USA* **79,** 2470–2474 (1982).
3. Marqusee, S., Robbins, V. H. & Baldwin, R. L. Unusually stable helix formation in short alanine-based peptides. *Proc Natl Acad Sci USA* **86,** 5286–5290 (1989).
4. Scholtz, J. M., Qian, H., York, E. J., Stewart, J. M. & Baldwin, R. L. Parameters of helix-coil transition theory for alanine-based peptides of varying chain lengths in water. *Biopolymers* **31,** 1463–1470 (1991).
5. Schellman, J. The factors affecting the stability of hydrogen-bonded polypeptide structures in solution. *The Journal of Physical Chemistry* (1958).
6. Muñoz, V. & Serrano, L. Elucidating the folding problem of helical peptides using empirical parameters. *Nat Struct Biol* **1,** 399–409 (1994).
7. Bustamante, C., Chemla, Y. R., Forde, N. R. & Izhaky, D. Mechanical processes in biochemistry. *Annu Rev Biochem* **73,** 705–748 (2004).
8. Sivaramakrishnan, S. *et al.* Combining single-molecule optical trapping and small-angle x-ray scattering measurements to compute the persistence length of a protein ER/K alpha-helix. *Biophys J* **97,** 2993–2999 (2009).
9. Jahn, R. & Scheller, R. H. SNAREs--engines for membrane fusion. *Nat Rev Mol Cell Biol* **7,** 631–643 (2006).
10. Cecconi, C., Shank, E. A., Bustamante, C. & Marqusee, S. Direct observation of the three-state folding of a single protein molecule. *Science* **309,** 2057–2060 (2005).
11. Shank, E. A., Cecconi, C., Dill, J. W., Marqusee, S. & Bustamante, C. The folding cooperativity of a protein is controlled by its chain topology. *Nature* **465,** 637–640 (2010).
12. Rief, M., Gautel, M., Oesterhelt, F., Fernandez, J. M. & Gaub, H. E. Reversible unfolding of individual titin immunoglobulin domains by AFM. *Science* **276,** 1109–1112 (1997).
13. Jagannathan, B. & Marqusee, S. Protein folding and unfolding under force. *Biopolymers* **99,** 860–869 (2013).
14. Liphardt, J., Onoa, B., Smith, S. B., Tinoco, I. & Bustamante, C. Reversible unfolding of single RNA molecules by mechanical force. *Science* **292,** 733–737 (2001).
15. Elms, P. J., Chodera, J. D., Bustamante, C. & Marqusee, S. The molten globule state is unusually deformable under mechanical force. *Proc Natl Acad Sci USA* **109,** 3796–3801 (2012).
16. Hollien, J. & Marqusee, S. A thermodynamic comparison of mesophilic and thermophilic ribonucleases H. *Biochemistry* **38,** 3831–3836 (1999).
17. Zoldák, G. & Rief, M. Force as a single molecule probe of multidimensional protein energy landscapes. *Curr Opin Struct Biol* **23,** 48–57 (2013).
18. Dietz, H., Berkemeier, F., Bertz, M. & Rief, M. Anisotropic deformation response

of single protein molecules. *Proc Natl Acad Sci USA* **103,** 12724–12728 (2006).

19. Gao, Y., Sirinakis, G. & Zhang, Y. Highly anisotropic stability and folding kinetics of a single coiled coil protein under mechanical tension. *J Am Chem Soc* **133,** 12749–12757 (2011).
20. Lee, W. *et al.* Mechanical anisotropy of ankyrin repeats. *Biophys J* **102,** 1118–1126 (2012).
21. Jagannathan, B., Elms, P. J., Bustamante, C. & Marqusee, S. Direct observation of a force-induced switch in the anisotropic mechanical unfolding pathway of a protein. *Proc Natl Acad Sci USA* **109,** 17820–17825 (2012).
22. Stigler, J., Ziegler, F., Gieseke, A., Gebhardt, J. C. M. & Rief, M. The complex folding network of single calmodulin molecules. *Science* **334,** 512–516 (2011).
23. Zheng, W. & Glenn, P. Probing the folded state and mechanical unfolding pathways of T4 lysozyme using all-atom and coarse-grained molecular simulation. *The Journal of chemical physics* **142,** 035101 (2015).
24. Bornschlögl, T. & Rief, M. Single-molecule protein unfolding and refolding using atomic force microscopy. *Methods Mol Biol* **783,** 233–250 (2011).
25. Yang, G. *et al.* Solid-state synthesis and mechanical unfolding of polymers of T4 lysozyme. *Proc Natl Acad Sci USA* **97,** 139–144 (2000).
26. Cecconi, C., Shank, E. A., Dahlquist, F. W., Marqusee, S. & Bustamante, C. Protein-DNA chimeras for single molecule mechanical folding studies with the optical tweezers. *Eur Biophys J* **37,** 729–738 (2008).
27. Tskhovrebova, L., Trinick, J., Sleep, J. A. & Simmons, R. M. Elasticity and unfolding of single molecules of the giant muscle protein titin. *Nature* **387,** 308–312 (1997).
28. Kellermayer, M. S., Smith, S. B., Granzier, H. L. & Bustamante, C. Folding-unfolding transitions in single titin molecules characterized with laser tweezers. *Science* **276,** 1112–1116 (1997).
29. Leake, M. C., Wilson, D., Gautel, M. & Simmons, R. M. The elasticity of single titin molecules using a two-bead optical tweezers assay. *Biophys J* **87,** 1112–1135 (2004).
30. Zhang, X., Halvorsen, K., Zhang, C.-Z., Wong, W. P. & Springer, T. A. Mechanoenzymatic cleavage of the ultralarge vascular protein von Willebrand factor. *Science* **324,** 1330–1334 (2009).
31. Jakobi, A. J., Mashaghi, A., Tans, S. J. & Huizinga, E. G. Calcium modulates force sensing by the von Willebrand factor A2 domain. *Nat Commun* **2,** 385 (2011).
32. Xu, A. J. & Springer, T. A. Calcium stabilizes the von Willebrand factor A2 domain by promoting refolding. *Proceedings of the National Academy of Sciences* **109,** 3742–3747 (2012).
33. Gebhardt, J. C. M., Bornschlögl, T. & Rief, M. Full distance-resolved folding energy landscape of one single protein molecule. *Proceedings of the National Academy of Sciences* **107,** 2013–2018 (2010).
34. Xi, Z., Gao, Y., Sirinakis, G., Guo, H. & Zhang, Y. Single-molecule observation of helix staggering, sliding, and coiled coil misfolding. *Proceedings of the National*

Academy of Sciences **109,** 5711–5716 (2012).

35. Dong, J., Castro, C. E., Boyce, M. C., Lang, M. J. & Lindquist, S. Optical trapping with high forces reveals unexpected behaviors of prion fibrils. *Nat Struct Mol Biol* **17,** 1422–1430 (2010).
36. Kaiser, C. M., Goldman, D. H., Chodera, J. D., Tinoco, I. & Bustamante, C. The ribosome modulates nascent protein folding. *Science* **334,** 1723–1727 (2011).
37. Heidarsson, P. O. *et al.* A highly compliant protein native state with a spontaneous-like mechanical unfolding pathway. *J Am Chem Soc* **134,** 17068–17075 (2012).
38. Yu, H. *et al.* Direct observation of multiple misfolding pathways in a single prion protein molecule. *Proceedings of the National Academy of Sciences* **109,** 5283–5288 (2012).
39. Gao, Y. *et al.* Single reconstituted neuronal SNARE complexes zipper in three distinct stages. *Science* **337,** 1340–1343 (2012).
40. Mashaghi, A. *et al.* Reshaping of the conformational search of a protein by the chaperone trigger factor. *Nature* **500,** 98–101 (2013).
41. Zoldák, G., Stigler, J., Pelz, B., Li, H. & Rief, M. Ultrafast folding kinetics and cooperativity of villin headpiece in single-molecule force spectroscopy. *Proc Natl Acad Sci USA* (2013). doi:10.1073/pnas.1311495110
42. Rognoni, L., Möst, T., Žoldák, G. & Rief, M. Force-dependent isomerization kinetics of a highly conserved proline switch modulates the mechanosensing region of filamin. *Proc Natl Acad Sci USA* **111,** 5568–5573 (2014).
43. Zorman, S. *et al.* Common intermediates and kinetics, but different energetics, in the assembly of SNARE proteins. *Elife* **3,** e03348 (2014).
44. Heidarsson, P. O. *et al.* Direct single-molecule observation of calcium-dependent misfolding in human neuronal calcium sensor-1. *Proc Natl Acad Sci USA* **111,** 13069–13074 (2014).
45. Guinn, E. J., Jagannathan, B. & Marqusee, S. Single-molecule chemo-mechanical unfolding reveals multiple transition state barriers in a small single-domain protein. *Nat Commun* **6,** 6861 (2015).
46. Afrin, R., Takahashi, I., Shiga, K. & Ikai, A. Tensile mechanics of alanine-based helical polypeptide: force spectroscopy versus computer simulations. *Biophys J* **96,** 1105–1114 (2009).
47. Berkemeier, F. *et al.* Fast-folding {alpha}-helices as reversible strain absorbers in the muscle protein myomesin. *Proc Natl Acad Sci USA* (2011). doi:10.1073/pnas.1105734108
48. Ferguson, N. & Fersht, A. R. Early events in protein folding. *Curr Opin Struct Biol* **13,** 75–81 (2003).
49. Lapidus, L., Steinbach, P. & Eaton, W. Effects of chain stiffness on the dynamics of loop formation in polypeptides. Appendix: Testing a 1-dimensional diffusion model for peptide dynamics. *The Journal of …* (2002).
50. Barlow, D. J. & Thornton, J. M. Helix geometry in proteins. *J Mol Biol* **201,** 601–619 (1988).
51. Wang, J. & Feng, J.-A. Exploring the sequence patterns in the alpha-helices of

proteins. *Protein Eng* **16,** 799–807 (2003).
52. Roy, R., Hohng, S. & Ha, T. A practical guide to single-molecule FRET. *Nat Methods* **5,** 507–516 (2008).
53. Gosse, C. & Croquette, V. Magnetic tweezers: micromanipulation and force measurement at the molecular level. *Biophys J* **82,** 3314–3329 (2002).
54. Lionnet, T. *et al.* Single-molecule studies using magnetic traps. *Cold Spring Harb Protoc* **2012,** 34–49 (2012).
55. van Loenhout, M. T. J., Kerssemakers, J. W. J., De Vlaminck, I. & Dekker, C. Non-bias-limited tracking of spherical particles, enabling nanometer resolution at low magnification. *Biophys J* **102,** 2362–2371 (2012).
56. Tarsa, P. B. *et al.* Detecting force-induced molecular transitions with fluorescence resonant energy transfer. *Angew Chem Int Ed Engl* **46,** 1999–2001 (2007).
57. Woodside, M. T. *et al.* Nanomechanical measurements of the sequence-dependent folding landscapes of single nucleic acid hairpins. *Proc Natl Acad Sci USA* **103,** 6190–6195 (2006).
58. Kiick, K. L., Saxon, E., Tirrell, D. A. & Bertozzi, C. R. Incorporation of azides into recombinant proteins for chemoselective modification by the Staudinger ligation. *Proc Natl Acad Sci USA* **99,** 19–24 (2002).
59. Wang, A., Winblade Nairn, N., Johnson, R. S., Tirrell, D. A. & Grabstein, K. Processing of N-terminal unnatural amino acids in recombinant human interferon-beta in Escherichia coli. *Chembiochem* **9,** 324–330 (2008).
60. Marks, I. S. *et al.* Strain-promoted ‘click’ chemistry for terminal labeling of DNA. *Bioconjug Chem* **22,** 1259–1263 (2011).
61. Link, A. J. & Tirrell, D. A. Cell surface labeling of Escherichia coli via copper(I)-catalyzed [3+2] cycloaddition. *J Am Chem Soc* **125,** 11164–11165 (2003).
62. Lipfert, J., Hao, X. & Dekker, N. H. Quantitative modeling and optimization of magnetic tweezers. *Biophys J* **96,** 5040–5049 (2009).
63. Velthuis, te, A. J. W., Kerssemakers, J. W. J., Lipfert, J. & Dekker, N. H. Quantitative guidelines for force calibration through spectral analysis of magnetic tweezers data. *Biophys J* **99,** 1292–1302 (2010).
64. Tanase, M., Biais, N. & Sheetz, M. Magnetic tweezers in cell biology. *Methods Cell Biol* **83,** 473–493 (2007).
65. Woodside, M. T. & Block, S. M. Reconstructing folding energy landscapes by single-molecule force spectroscopy. *Annu Rev Biophys* **43,** 19–39 (2014).
66. Hoffman, B. D., Grashoff, C. & Schwartz, M. A. Dynamic molecular processes mediate cellular mechanotransduction. *Nature* **475,** 316–323 (2011).
67. Bustamante, C., Marko, J. F., Siggia, E. D. & Smith, S. Entropic elasticity of lambda-phage DNA. *Science* **265,** 1599–1600 (1994).
68. Marqusee, S. & Baldwin, R. L. Helix stabilization by Glu-...Lys+ salt bridges in short peptides of de novo design. *Proc Natl Acad Sci USA* **84,** 8898–8902 (1987).
69. Baker, E. G. *et al.* Local and macroscopic electrostatic interactions in single α-helices. *Nat Chem Biol* **11,** 221–228 (2015).
70. Muñoz, V. & Serrano, L. Elucidating the folding problem of helical peptides using empirical parameters. II. Helix macrodipole effects and rational modification of the

helical content of natural peptides. *J Mol Biol* **245,** 275–296 (1995).

71. Muñoz, V. & Serrano, L. Elucidating the folding problem of helical peptides using empirical parameters. III. Temperature and pH dependence. *J Mol Biol* **245,** 297–308 (1995).
72. Muñoz, V. & Serrano, L. Development of the multiple sequence approximation within the AGADIR model of alpha-helix formation: comparison with Zimm-Bragg and Lifson-Roig formalisms. *Biopolymers* **41,** 495–509 (1997).
73. Lacroix, E., Viguera, A. R. & Serrano, L. Elucidating the folding problem of alpha-helices: local motifs, long-range electrostatics, ionic-strength dependence and prediction of NMR parameters. *J Mol Biol* **284,** 173–191 (1998).
74. Krüger, A. C. & Birkedal, V. Single molecule FRET data analysis procedures for FRET efficiency determination: probing the conformations of nucleic acid structures. *Methods* **64,** 36–42 (2013).
75. Sabanayagam, C. R., Eid, J. S. & Meller, A. Using fluorescence resonance energy transfer to measure distances along individual DNA molecules: corrections due to nonideal transfer. *The Journal of chemical physics* **122,** 061103 (2005).
76. Torabi, K. & Schatz, G. Tensile Mechanics of α-Helical Polypeptides. *Macromolecules* (2013).
77. Holden, S. J. *et al.* Defining the limits of single-molecule FRET resolution in TIRF microscopy. *Biophys J* **99,** 3102–3111 (2010).